
Improving the Reconstruction of Disentangled Representation Learners via Multi-Stage Modeling

Akash Srivastava, Yamini Bansal, Yukun Ding, Cole Lincoln Hurwitz
Equal Contribution
MIT-IBM Watson AI Lab
Cambridge, MA

**Kai Xu, Bernhard Egger, Prasanna Sattigeri, Joshua B. Tenenbaum, Kristjan Greenewald,
David D. Cox, Dan Gutfreund**
MIT-IBM Watson AI Lab, IBM Research, MIT
Cambridge, MA

**Agus Sudjianto, Phuong Le, Arun Prakash R, Nengfeng Zhou, Joel Vaughan; Yaqun Wang,
Anwasha Bhattacharyya ***
Wells Fargo, US

Abstract

Current autoencoder-based disentangled representation learning methods achieve disentanglement by penalizing the (aggregate) posterior to encourage statistical independence of the latent factors. This approach introduces a trade-off between disentangled representation learning and reconstruction quality since the model does not have enough capacity to learn correlated latent variables that capture detail information present in most image data. To overcome this trade-off, we present a novel multi-stage modeling approach where the disentangled factors are first learned using a penalty-based disentangled representation learning method; then, the low-quality reconstruction is improved with another deep generative model that is trained to model the missing correlated latent variables, adding detail information while maintaining conditioning on the previously learned disentangled factors. Taken together, our multi-stage modelling approach results in a single, coherent probabilistic model that is theoretically justified by the principal of D-separation and can be realized with a variety of model classes including likelihood-based models such as variational autoencoders, implicit models such as generative adversarial networks, and tractable models like normalizing flows or mixtures of Gaussians. We demonstrate that our multi-stage model has higher reconstruction quality than current state-of-the-art methods with equivalent disentanglement performance across multiple standard benchmarks. In addition, we apply the multi-stage model to generate synthetic tabular datasets, showcasing an enhanced performance over benchmark models across a variety of metrics. The interpretability analysis further indicates that the multi-stage model can effectively uncover distinct and meaningful features of variations from which the original distribution can be recovered.

*The authors from Wells Fargo express their gratitude to Yueyang Shen and Maorong Rao for their valuable contributions to the discussion. Appreciation is also extended to the corporate risk - model risk team at Wells Fargo for their support in this project. The views expressed in the paper are those of the authors and do not represent the views of Wells Fargo.

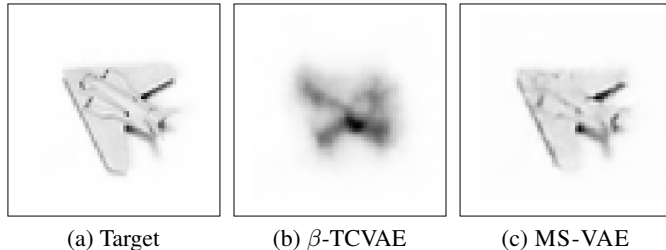


Figure 1: Image reconstruction using β -TCVAE (Figure 1b) and MS-VAE (Figure 1c). MS-VAE is able to take the blurry output of the underlying β -TCVAE model and learn to render a much better approximation of the target while maintaining the pose of the original image (Figure 1a).

1 Introduction

Deep generative models (DGMs) such as variational autoencoders (VAEs) (Kingma & Welling, 2014; Rezende et al., 2014) and generative adversarial networks (GANs) (Goodfellow et al., 2014) have recently enjoyed great success at modeling high dimensional data such as natural images. As the name suggests, DGMs leverage deep learning to model a data generating process. The underlying assumption is that the high dimensional observations $X \in \mathbb{R}^D$ can be meaningfully described by a small set of latent factors $H \in \mathbb{R}^K$, where $K < D$. More precisely, the observation ($X = x$) is assumed to be generated by first sampling a set of low dimensional factors h from a simple prior distribution $p(H)$ and then sampling $x \sim p_\theta(X|h)$. DGMs realize p_θ through a deep neural network also known as the decoder or the generative network. VAE-based DGMs use another deep neural network (called the encoder or the inference network) to parameterize an approximate posterior $q_\phi(H|x)$. Learning the variational posterior parameters is done by maximizing an evidence lower bound (ELBO) to the log-marginal likelihood of the data under the model $p_\theta(X)$.

Learning *disentangled* factors $h \sim q_\phi(H|x)$ that are semantically meaningful representations of the observation x is highly desirable because such interpretable representations can arguably be advantageous for a variety of downstream tasks (Locatello et al., 2018), including classification, detection, reinforcement learning, transfer learning and image synthesis from textual descriptions (Bengio et al., 2013; LeCun et al., 2015; Lake et al., 2017; van Steenkiste et al., 2019; Reed et al., 2016; Zhang et al., 2016). While a formal definition of disentangled representation (DR) remains elusive, it is understood to mean that by manipulating only one of the factors while holding the rest constant, only one semantically meaningful aspect of the observation (e.g. the pose of an object in an image) changes. Prior work in unsupervised DR learning focuses on the objective of learning statistically independent latent factors as means for obtaining DR. The underlying assumption is that the latent variables H can be partitioned into independent components C (i.e. the disentangled factors) and correlated components Z . An observation ($X = x$) is assumed to be generated by sampling the low dimensional factors $h = (c, z)$ from $p(H)$ and then sampling $x \sim p_\theta(X|c, z)$ (Figure 2a). A series of works starting from (Higgins et al., 2017) enforce statistical independence of the latent factors H via regularization, up-weighting certain terms in the ELBO which penalize the (aggregate) posterior to be factorized over all or some of the latent dimensions (Kumar et al., 2017; Kim & Mnih, 2018; Chen et al., 2018) (see Section 2 for details).

While the aforementioned models show promising results, they suffer from a trade-off between DR learning and reconstruction quality. If the latent space is heavily regularized – not allowing enough capacity for the correlated variables – then the reconstruction quality will be diminished, signaling that the learned representation is sub-optimal. As the correlated variables are functionally ignored with high levels of regularization, an observation ($X = x$) can be thought to be generated by only sampling independent latent factors c from $p(C)$ and then sampling $x \sim p_\theta(X|c)$ (Figure 2b). This is a departure from the original data generating hypothesis that x is sampled from a distribution dependent on both the independent and correlated latent variables. On the other hand, if the correlated variables are not well-constrained, the model can use them to achieve a high quality reconstruction while ignoring the independent variables (the disentangled latent factors). This phenomena is referred to as the "shortcut problem" and has been discussed in previous works (Szabó et al., 2018; Lezama, 2018). Overcoming the aforementioned trade-off is essential for using these models in real world applications such as realistic, controlled image synthesis (Lee et al., 2020; Lezama, 2018).

In this paper, we propose a new graphical model for DR learning (Figure 2c) that allows for learning disentangled factors while also correctly realizing the data generating hypothesis that an observation is generated from independent and correlated factors. Importantly, the graphical model in Figure 2c is D-separated, meaning that any changes in the correlated latent variables Z will not influence the independent latent variables C . Generating an observation ($X = x$) from this model can then be done by sampling the independent factors c from $p(C)$, sampling a low-quality reconstruction $y \sim p_\theta(Y|c)$, sampling the correlated factors z from $p(Z)$, and then finally sampling $x \sim p_\theta(X|z, Y)$. The final reconstruction x depends both on z and c , however, any regularization needed to extract the independent factors c no longer diminishes the model capacity for the correlated factors z .

To realize our proposed graphical model, we introduce **MS-VAE**, a multi-stage DGM that is implemented as follows: first, the disentangled representation C is learned using an existing DR learning method such as β -TCVAE (Chen et al., 2018). Since the learned factors C are regularized to be statistically independent – not allowing enough capacity for correlated factors – the final reconstruction Y will have diminished reconstruction quality. Then, we train another DGM to improve the low-quality reconstruction Y by learning the missing correlated factors Z . This is achieved during training by inputting the reconstruction Y into the decoder of the second DGM and then modulating the hidden activation of each layer as function of latent factor Z (using Feature-wise Linear Modulation (Perez et al., 2018)). Through this training paradigm, MS-VAE is able to preserve conditioning on the disentangled factors while dramatically improving the reconstruction quality. A schematic of MS-VAE is shown in Figure 2d and example images from each stage are shown in Figure 1. The reconstruction from β -TCVAE (1b) is improved by MS-VAE (1c) to better approximate the target (1a) while maintaining conditioning on the disentangled factors, e.g. azimuth.

To summarize our contributions:

- We propose a new graphical model for DR learning (Figure 2c) that, due to the D-separation between its independent and correlated latent variables, alleviates the disentanglement vs. reconstruction trade-off.
- We introduce MS-VAE, a multi-stage DGM that implements our proposed graphical model, achieving state-of-the-art reconstruction quality while maintaining the same level of disentanglement as preexisting methods. MS-VAE can be implemented using a variety of DGMs such as VAEs, GANs, or FLOW-based models and does not depend on hand-crafted loss functions or additional hyperparameters (unlike current state-of-the-art (Lezama, 2018))
- Following (Locatello et al., 2018), we test our framework with a wide-range of qualitative and quantitative tests to demonstrate the efficacy of the framework. We provide all code used for the experiments.

2 Background

VAEs, first introduced in (Kingma & Welling, 2014), represent a class of likelihood-based, DGMs comprised of an encoder and a decoder that are trained using amortized variational inference to maximize the expected ELBO under the data distribution,

$$\int p(x) \log p_\theta(x) dx \geq \mathbb{E}_{p(x)} [\mathbb{E}_{q_\phi(h|x)} [\log p_\theta(x|h)] - \text{KL}[q_\phi(h|x)||p(h)]] \quad (1)$$

The first term is the expected reconstruction loss under the variational posterior q_ϕ . The second term – the Kullback–Leibler (KL) divergence – underpins most of the recent DR learning methods. The KL term regularizes the variational posterior to be similar (in expectation) to a simple spherical Gaussian prior over H . Higgins et al. (2017) attempts to factorize the variational aggregate posterior by up-weighting this KL-divergence term with a Lagrange multiplier β . Follow-up works decompose the KL-term in equation 1 and up-weight only the KL-divergence between the aggregate posterior $q_{\phi_H}(H) = \int_X p(x)q_\phi(H|x)dx$ and the factorized aggregate posterior (Kim & Mnih, 2018; Chen et al., 2018; Jeong & Song, 2019). Kumar et al. (2017) simply uses a factorized prior. These models introduce a trade-off between unsupervised DR learning and reconstruction quality. When the latent variables are heavily regularized to be independent, an observation ($X = x$) can be thought to be generated by sampling independent latent factors c from $p(C)$ and then sampling $x \sim p_\theta(X|c)$ (Figure 2b). This leads to low-quality reconstructions as the correlated factors are not utilized. Lezama (2018) attempts to tackle this issue with a teacher-student learning technique. First, the

teacher model is trained to extract disentangled factors at the cost of reconstruction quality (similar to the first stage of our model). Then, a student autoencoder (AE) model with a larger latent dimension size is trained with additional losses that force the Jacobian of the final reconstruction with respect to the disentangled factors to remain the same (a.k.a Jacobian supervision). While this model achieves promising results on MNIST (Deng, 2012), it suffers from a few drawbacks including having to relearn the disentangled factors in the second stage and having no theoretical guarantees that changes in the correlated factors Z will not affect the independent factors C in the student model. Other works have also been proposed to overcome the trade-off using adversarial training (Mathieu et al., 2016; Lample et al., 2017; Perarnau et al., 2016; Szabó et al., 2018; Hu et al., 2018).

3 Method

3.1 Graphical Model

Lower Bound. To alleviate the trade-off between reconstruction and disentanglement, we propose a new graphical model for DR learning (Figure 2c). To understand this model, let us assume that the data come as pairs of images $\{y_i, x_i\}_{i=1}^N$. Let the x 's be the ground truth images (generated using both the independent factors c and correlated factors z) and let the y 's be the approximations of those images generated using only c . Given this paired data, the graphical model depicted in Figure 2c represents a single coherent model of the data that defines a joint distribution over Y and X . The log-marginal likelihood of the observations under this model can be lower-bounded as follows,

$$\begin{aligned} \log p_{\{\phi, \theta, \theta_Z, \Theta\}}(x, y) \geq & \quad (2) \\ & \underbrace{-\text{KL}[q_\phi(c|y)||p(c)] + \mathbb{E}_{q_\phi}[\log p_\theta(y|c)]}_{(a) C \rightarrow Y} - \underbrace{\text{KL}[q_{\theta_Z}(z|x, y)||p(z)] + \mathbb{E}_{q_{\theta_Z}}[\log p_\Theta(x|z, y)]}_{(b) (Y, Z) \rightarrow X}. \end{aligned}$$

In practice, we do not have access to Y . However, by learning the disentangled factors C from X , we can generate Y . Therefore, we first use state-of-the-art DR learning method to learn the sub-graph $C \rightarrow Y$ by maximizing term (a) in Equation 2 to produce Y . Then, we train another DGM to learn the sub-graph $(Y, Z) \rightarrow X$ by maximizing term (b) in Equation 2. This two-stage training procedure approximates the graphical model from Figure 2c.

D-separation. Now that we introduced the graphical model from Figure 2c, it is important to understand the theoretical motivation behind it. Recall that our goal is to take an existing method for learning the disentangled factors C and learn additional residual information in Z without changing the conditioning on C . In a standard VAE graphical model (Figure 2a), this could occur because there is no guarantee that $p(Z, C|X) = p(Z|X)p(C|X)$. By introducing an observed node Y (i.e. D-Separation) in our graphical model, we ensure that changes in Z will not influence C . This is because the joint distribution $p(Z, C|X, Y)$ can now be broken down as $p(C|Y)p(Z|X, Y)$. We illustrate this property of the graphical model with a toy example (Appendix L). In practice, realizing the graphical model in Figure 2c using a deep neural network requires care as we want to ensure that the conditioning on Y is stronger than that of Z so that Z only captures the residual correlated information. Also, simply training a single neural network end-to-end to approximate this graphical model is infeasible as Y will no longer act as an observed node, leading to the entanglement of C and Z . We demonstrate this phenomenon by performing an ablation study of our proposed method (Appendix M).

3.2 Implementation (MS-VAE)

In the following sections, we describe how the graphical model in Figure 2c can be implemented as variational autoencoder using a multi-stage modelling approach, i.e. MS-VAE.

Stage one: Learning a Disentangled Representation. In stage one, we train a penalty-based DR learning method to infer the independent latent factors C . Although this stage can be realized with any penalty-based method, we utilize β -TCVAE (Chen et al., 2018) to learn the independent latent factors because it has been shown to perform well across all standard benchmarks and its total correlation penalty is simpler to compute in comparison to FactorVAE's (Kim & Mnih, 2018). We use the standard convolution and transposed-convolutions-based realization of β -TCVAE as provided

in the *disentanglement_lib* (Locatello et al., 2018) package. As β -TCVAE heavily regularizes the latent space to be statistically independent – not allowing enough capacity for the correlated factors – the final reconstruction Y will be low-quality.

Stage Two: Improving the Reconstruction. In stage two, we learn the correlated factors Z with another DGM and then use them to improve the reconstruction Y while maintaining the conditioning on the independent factors C . To this end, we train a conditional VAE that models the data X given Y and Z . The encoder network R_{θ_Z} learns the posterior distribution over Z as a function of the residual of X and Y . The observation model G_{Θ} then reconstructs X given Y and Z . Incorporating Z into G_{Θ} requires care as simply inputting the concatenation of Y and Z into the network at the start of training will result in a non-linear entanglement between Y and Z . Once entangled this way, G_{Θ} will fail to condition on Y sufficiently and use the entangled representation as a whole towards the reconstruction of X . To overcome this, we induce an architectural bias with a Feature-wise Linear Modulation (FiLM) technique (Perez et al., 2017) prevalent in style transfer literature (Huang & Belongie, 2017), introducing Z only through the adaptive instance normalization (AdaIN) layers of G_{Θ} . As demonstrated in Dumoulin et al. (2018), inputting Y into the decoder and then incorporating Z through AdaIN at each layer allows the network to use Z later in the generative process to model the residual information. This allows the network to better preserve the information in Y while improving the reconstruction with Z . We demonstrate the importance of AdaIN by performing an ablation study of MS-VAE (Appendix M).

FiLM and AdaIN. Recently, FiLM have been proposed as a general-purpose conditioning technique for deep neural networks (Perez et al., 2018). A FiLM layer learns an affine transformation of the intermediate statistics of a deep neural network, conditioned on an external input. FiLM has found great success in style transfer literature where the goal is to render content from a source domain in the style of a target domain. One such method, Instance Normalization (Ulyanov et al., 2016), incorporates the style and the content information through the normalization layers in a feed-forward network, learning style-specific affine parameters from the data that are used to shift and scale the feature statistics (per instance) extracted from the source image across spatial dimensions. Huang & Belongie (2017) extended this method to address arbitrary styles by taking the affine parameters to be the feature statistics extracted from the style domain, arriving at the $AdaIN(y, x) = \sigma(x) \left(\frac{y - \mu(y)}{\sigma(y)} \right) + \mu(x)$ which is applied for each normalization layer. Here, y are the incoming activations for a normalization layer in the network that is receiving an image from the source domain and x are the style features computed from the target domain. The features statistics for y (as well as for x) are computed as follows: $\mu(y) = \frac{1}{HW} \sum_{h,w} a_{nhwc}$ and $\sigma(y) = \sqrt{\frac{1}{HW} \sum_{h,w} (x_{nhwc} - \mu(y))^2 + \epsilon}$, where h, w, c stand for the height, width and channel, respectively. In MS-VAE, the equivalent of style features is the representation of the residual information between X and Y captured in the correlated variables Z . The goal is similar to style transfer: incorporate the information stored in Z while maintaining the semantic content stored in Y . Therefore, we slightly modify the AdaIN formulation as follows: $AdaIN(y, z) = \gamma(z) \left(\frac{y - \mu(y)}{\sigma(y)} \right) + \beta(z)$. where $\mu(y)$ and $\sigma(y)$ are the same as before and $\gamma(z)$ and $\beta(z)$ are learned functions of z parameterized by a fully-connected neural network. As mentioned before, incorporating Z through AdaIN at each layer allows the network to use Z later in the generative process to model the residual information, thus preserving the information in Y (Dumoulin et al., 2018).

MS-GAN. Equation 2 also allows for realizing subgraph $(Y, Z) \rightarrow X$ using a GAN, with a little manipulation. Simply by adding and subtracting the log of the true conditional density $\log p(X|Y)$ in equation 2, we get the lower bound,

$$\log p_{\{\phi, \theta, \theta_Z, \Theta\}}(x, y) \geq -\mathcal{KL}[q_{\phi}(c|y) \| p(c)] + \int q_{\phi}(c|y) \log p_{\theta}(y|c) dc - \mathcal{KL}[q_{\theta_Z}(z|x, y) \| p(z)] + \underbrace{\int q_{\theta_Z}(z|x, y) \log \frac{p_{\Theta}(x|z, y)}{p(x|y)} dz}_{\text{CGAN-based } (Y, Z) \rightarrow X} + \log p(x|y) \quad (3)$$

Here, the log density ratio $\log \frac{p_{\Theta}(x|z, y)}{p(x|y)}$ can be estimated using adversarial learning with a binary discriminator function (Sugiyama et al., 2012; Srivastava et al., 2017). In practice, since we are learning conditional distributions, the decoder is implemented as a conditional GAN (CGAN) Mirza &

Osindero (2014). We refer to this implementation as MS-GAN. We show that MS-GAN leads to even higher fidelity generation than MS-VAE while delivering better disentanglement than conditional GAN. We also qualitatively compare MS-GAN to the InfoGAN model (Chen et al., 2016) for the unsupervised DR learning. Due to space constraints, we defer the details and all the results of this study to the Appendix F.

MS-FLOW. We also present a simple a FLOW-based version of our framework, MS-FLOW, that utilizes a mixture of Gaussians model to realize the sub-graph $C \rightarrow Y$ and a flow-based model to realize the subgraph $(Y, Z) \rightarrow X$. The flow-based model in MS-VAE can be implemented as a conditional normalizing flow that conditions on Y Dinh et al. (2014); Huang et al. (2018); Durkan et al. (2019). As we are limited for space, we defer the details of the model and the experiment results to the Appendix E.

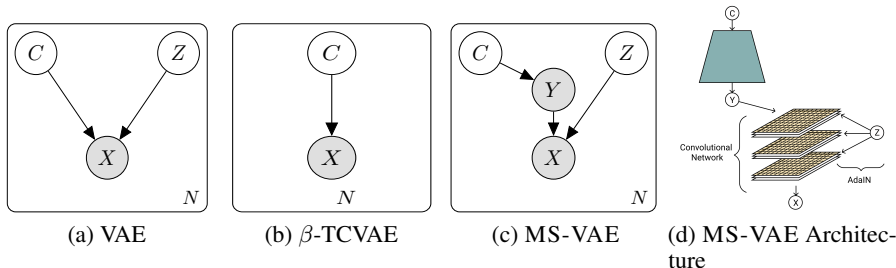


Figure 2: (a) Graphical model of a standard VAE where C and Z are not independent conditioned on X . (b) Graphical model of β -TCVAE where the reconstruction only depends on the independent latent factors C . (c) MS-VAE graphical model where C and Z are independent conditioned on Y . (d) Schematic for MS-VAE when implemented as a convolutional architecture. Both Y and X are the reconstructions of the same image.

4 Experiments

Baseline Models Locatello et al. (2018) demonstrated that most state-of-the-art DR learning methods are able to effectively learn a factorized posterior distribution (i.e. extract independent latent variables C). Therefore, we chose β -TCVAE as the baseline DR learning method for our paper. For fair comparison with our work, we use β -TCVAE to implement the sub-graph $C \rightarrow Y$ in MS-VAE. For our main experiments, we thoroughly evaluate three models: (i) MS-VAE with latent dimensions C for the $C \rightarrow Y$ network and Z for the $(Y, Z) \rightarrow X$ network, (ii) β -TCVAE with latent dimension size $|C|$, and (iii) β -TCVAE-L with latent dimension size $|C + Z|$. In line with previous work (Locatello et al., 2018), we use a 10-dimensional C . We use a 5-dimensional and 10-dimensional Z for *Cars3D* and *SmallNorb*, respectively. In Appendix B, we sweep over the dimensionalities of C and Z to evaluate its effect on the reported results. We train β -TCVAE with β values ranging from 1 to 10. In addition to the main models, we include comparisons to a recent state-of-the-art method, Jacobian Supervision (Lezama, 2018). Although Jacobian supervision can be implemented with multiple student autoencoders, we only compare to the single student model version as it is most directly comparable to MS-VAE. We utilize the same architecture and C, Z dimensionalities as MS-VAE. For their teacher model, we also use a pre-trained β -TCVAE model as we did for MS-VAE, but we only evaluate their method for $\beta = 1, 10$. The hyperparameters and loss functions are as specified in the paper and are available in the linked code repository.

Measuring Disentanglement Performance Locatello et al. (2018) concluded that most metrics for measuring disentanglement performance correlate relatively well with each other. Therefore, we only use MIG (Chen et al., 2018) to quantitatively measure disentanglement performance. Please see Appendix H for how this is computed.

Measuring Reconstruction Quality. Following (Razavi et al., 2019), we report the Frchet Inception Distance (FID) (Heusel et al., 2017) between the dataset and each models’ reconstructions. We choose FID instead of reconstruction error for our main metric as L1/L2 metrics are known to not correlate well with perceived image quality (Wang et al., 2003, 2004). We still report both L1 and L2

results in Appendix K. Additionally, FID does not require a well-defined likelihood function and can, therefore, be used to evaluate MS-VAE when the conditional model is implemented using a GAN.

Measuring the Conditioning on C . To quantitatively measure how well the improved reconstructions are conditioned on the independent latent variables C , we use the following procedure. Let the mean parameter of the encoder of the subgraph $C \rightarrow Y$ be E_ϕ . Further, let $C_R = E_\phi(X)$, $C_Y = E_\phi(Y)$, $C_X = E_\phi(G_\Theta(Y, Z))$, $C_{z_\epsilon} = E_\phi(G_\Theta(Y, \epsilon))$, and $C_{Y_\epsilon} = E_\phi(G_\Theta(\epsilon, Z))$ where X is an input image, $\epsilon \sim \mathcal{N}(0, I)$, and G_Θ is the decoder of the second stage of MS-VAE. We report the following mutual information terms: $M_1 = \text{MI}[C_R; C_Y]$, $M_2 = \text{MI}[C_R; C_X]$, $M_3 = \text{MI}[C_R; C_{z_\epsilon}]$, and $M_4 = \text{MI}[C_R; C_{Y_\epsilon}]$. If Z is encoding meaningful information for the reconstruction process then we should see $M_2 > M_1$ as the reconstruction should better approximate the ground truth image X . More importantly, if $M_1 > M_3 \gg M_4$ then the conditioning on Y (and therefore C) can be assumed to be maintained. This follows because if G_Θ was only using Z for the final reconstruction, M_3 would be close to zero and M_4 would be high (since Y is not being used in the final reconstruction). In addition to this quantitative analysis, we provide latent traversal plots for all the datasets to qualitatively show that the conditioning on the disentangled factors C is preserved.

Downstream Classification To demonstrate that Z is learning meaningful residual information that is *complementary* to C , we perform a set of downstream classification tasks using both Z and C . In these tasks, we predict attributes of objects in the *SmallNORB* dataset using an MLP that is trained with three different inputs: C , Z , and both C and Z concatenated together. Ideally, the MLP trained with both C and Z would achieve the highest accuracy as the inferred latent variables contain complementary information about the object attributes.

Ablation Studies MS-VAE design employs four major modelling choices. In order to explain their individual impact on the model, we carried out a set of empirical analysis. Specifically, we performed ablation studies to understand the contribution of: (1) Our two-step training paradigm (vs end-to-end training). (2) Our use of Y instead of C for the second stage (vs the underlying graphical model of ID-GAN Lee et al. (2020)). (3) Our use of AdaIN to incorporate Z . (4) Our decision to learn C before learning Z . To evaluate our two-step training process, we compare MS-VAE to a model where both the C and Z factors are learned together in an end-to-end manner (by penalizing only C) and Z is incorporated using AdaIN. To evaluate how using Y improves reconstruction performance over using C , we compare MS-VAE to a version of MS-VAE where Y is replaced with C . To evaluate the contribution of AdaIN for disentanglement, we compare MS-VAE to a version of MS-VAE where C and Z are concatenated together as input to the second stage DGM. Finally, to evaluate our decision to learn C before learning Z , we train a version of MS-VAE where Z is learned in the first stage and then C is learned in the second stage (C and Z are concatenated together to reconstruct X). Due to space constraints, all experiments are reported in the Appendix M.

Code and Datasets. We use the *disentanglement_lib* package (Locatello et al., 2018) to train all β -TCVAE models and to evaluate MIG. The datasets we use for our quantitative benchmarks are *Cars3D* (Reed et al., 2015) and *SmallNORB* (LeCun et al., 2004). These datasets are a subset of those used in the large scale study of (Locatello et al., 2018) and are available (with ground truth factors) from the *disentanglement_lib* package. Additionally, we use the CelebA (Liu et al.) dataset of real face images for qualitative evaluations since the other datasets consist of only simulated images (see Appendix C). For FID evaluations, we use the standard Tensorflow (Abadi et al., 2016) implementation for all the models. We provide all the hyperparameter and architectural details for the experiments in the appendix. A reference Tensorflow implementation is also available at <https://github.com/AnonymousAuthors000/DS-VAE> in the form of a Jupyter notebook.

5 Results on Computer Vision Datasets

Disentanglement Performance. As mentioned above, MS-VAE utilizes β -TCVAE to learn disentangled factors in the first stage of its training. Therefore, we report the MIG values for the β -TCVAE used with MS-VAE and for β -TCVAE-L (a β -TCVAE with the same latent dimension as MS-VAE). For the *Cars3D* dataset, we find that with both models, the MIG scores increase as β is increased (Figure 3a(ii)). However, β -TCVAE appears to consistently have a higher MIG than β -TCVAE-L, potentially reflecting the entangling effect of an overly large latent space. For the *SmallNORB* dataset, MIG decreases as the value of β increases as shown in Figure 3b(ii). This confirms the findings of Locatello et al. (2018) on this particular dataset. Overall, these results illustrate that MS-VAE is

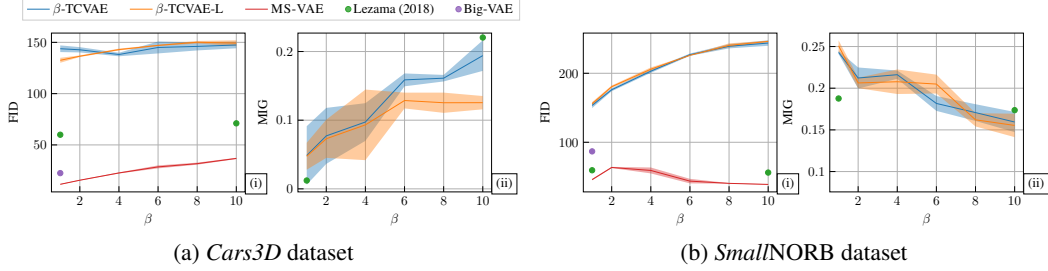


Figure 3: FID (lower is better) and MIG (higher is better) comparison of β -TCVAE, β -TCVAE-L, and MS-VAE models. On both datasets, MS-VAE is able to consistently improve the reconstruction quality of its underlying β -TCVAE model while achieving a better MIG than β -TCVAE-L. We also provide FID and MIG results for Lezama’s model (Lezama, 2018) with $\beta = 1, 10$ as well as FID for a vanilla VAE model of the same capacity as MS-VAE (denoted Big-VAE).

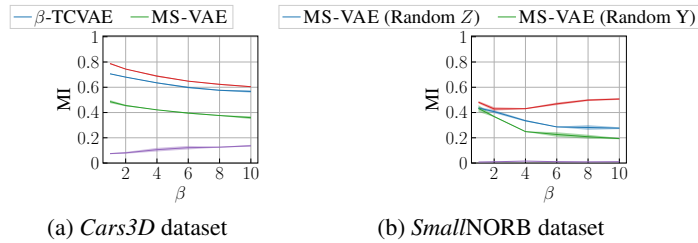


Figure 4: Mutual Information (MI) between inferred independent factors from the true image X (using β -TCVAE) and independent factors from various reconstructions of X . Please note that Blue = M_1 , Red = M_2 , Green = M_3 , and Purple = M_4 (see Section 4 for their definitions).

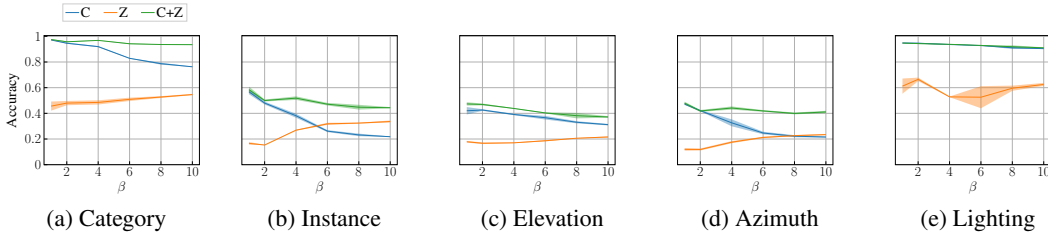


Figure 5: Object property prediction for *SmallNORB* using inferred representations C , Z , and $C + Z$ as input to a MLP. The accuracy is highest for the MLP trained with $C + Z$.

able to extract disentangled factors from image data at the same level as state-of-the-art methods and that naively increasing the latent dimensionality of β -TCVAE may diminish disentanglement performance. For the Jacobian supervision baseline (Lezama, 2018), we use β -TCVAE at the teacher model with two values of β (1 and 10). After training, the MIG values for the student network are approximately the same as teacher model on both datasets (i.e. it maintains disentanglement).

Reconstruction Quality. As shown in Figures 3a(i) and 3b(i), MS-VAE drastically improves the reconstruction quality compared to both β -TCVAE models, achieving a much lower FID across all values of β . We also compare MS-VAE to Jacobian supervision and find that MS-VAE has lower FID on both datasets. To ensure that the improvement in reconstruction quality over β -TCVAE is not just because MS-VAE has more parameters, we trained several β -TCVAE models with the same number of parameters as MS-VAE on the *SmallNORB* dataset and reported the results in Appendix I. Although we found marginal improvements in the average FID for these bigger β -TCVAEs (145.79 ± 2.98), they are still far higher than MS-VAE’s FID (59.16 ± 4.52). Also, increasing the parameters of β -TCVAE led to a decreased MIG (0.163 ± 0.026) which indicates that increasing the parameters of β -TCVAE may increase reconstruction quality at the cost of disentanglement. Finally, for reference, we provide FID scores for a standard VAE with same number of parameters as MS-VAE (we refer to this model as Big-VAE). Surprisingly, MS-VAE has a lower FID than

Big-VAE at low values of β suggesting that the residual modeling in MS-VAE leads to better image quality in general (see Figures 3a(i) and 3b(i)).

Conditioning on C Consider Figures 4a and 4b where we report the mutual information terms M_1, M_2, M_3 , and M_4 for both datasets (see Section 4 for their definitions). As per our expectation, we find that $M_2 > M_1 > M_3 \gg M_4$ and that M_3 tracks M_1 without dropping significantly. This suggests that Z is encoding meaningful information for the reconstruction of X and that the model maintains the conditioning on C in the final reconstruction. We further illustrate the conditioning on the C with qualitative examples. In Figures 13(c), 13(d) and 13(e) in the Appendix A, we show latent traversal of Y and X pairs. Notice, MS-VAE improves the quality of the generated output without diminishing the ability of the model to manipulate single factors of variation by traversing C .

Downstream Classification The results of the downstream attribute prediction tasks are shown in Figure 5. As can be seen, the MLP that was trained with both C and Z attains a higher accuracy on all five attribute prediction tasks than the MLPs trained with only C or Z . Notice that as the regularization of the latent space increases (larger β) and the accuracy of the classifier trained on C decreases, the accuracy of the classifier trained on Z increases. This highlights that Z contains complementary information to that of C and sheds light on why simply increasing the size of the latent space (i.e. the β TCVAE-L model) does not improve the reconstruction significantly.

6 Experiments with tabular data generation

Synthetic data generation is an important topic at the intersection of machine learning and finance. The generated data can be used for critical downstream tasks such as fraud detection or customer propensity prediction. Moreover, such generated data is especially useful when the real data is limited or too sparse and irregular to be used for machine learning training.

Variational autoencoder (VAE) and its variations proved to be highly effective in data generation tasks on many types of data ranging from images to structured data such as molecules. Nonetheless, applying VAE to tabular data, which frequently appears in financial domains, is a non-trivial task. Many VAE models used for tabular data-related work tend to be in the healthcare domain (Yahi et al. (2017); Choi et al. (2017)).

Often, the mechanism for data generation of VAE from the latent space is hidden and can only be accessed via the weights of the neural network. To allow interpretability for financial compliance and regulations, one needs to provide meaningful descriptions of each coordinate of the latent space. Moreover, we also expect that those coordinates can reflect the core factors underlying the original input data.

As a result, we are motivated to consider VAE models that can handle these two problems: TVAE (Xu et al. (2019)), β -TCVAE (Chen et al., 2018), and MS-VAE. In this section, we apply these three models to generate synthetic credit tabular data, evaluate their performance, and analyze the corresponding latent features learned. Our goals are to explore and detect appropriate latent representation models for data generation tasks in the financial domain. The details of the experiments on credit tabular data are provided together with comprehensive model evaluation and analysis. Furthermore, we dedicate Section 7 to investigating how the two models β -TCVAE and MS-VAE allow interpretability for data transparency purposes.

6.1 Baseline modes TVAE

Variational autoencoder was first developed to work on real-valued data, often image data. However, modeling the probability distribution of rows in tabular data and generating realistic synthetic data with VAE is a non-trivial task. Xu et al. (2019) develop TVAE framework to handle this task where tabular data contain a mixture of discrete and continuous variables. For discrete variables, Xu et al. (2019) uses the standard one-hot encoding, while the authors use mode-specific normalization to handle continuous feature columns. More specifically, TVAE models each continuous variable by a Gaussian mixture model so that each variable is represented by a pair of number (α, β) . Here, β indicates which Gaussian mode the variable belongs to and α is the normalized value of this variable w.r.t the chosen mode. TVAE’s neural network architectures for encoder and decoder are then modified to represent the real variable α , the distribution vectors for discrete variables, and β ’s values of continuous variables.

6.2 Experimental setup

Datasets. We apply 3 methods TVAE, β -TCVAE and MS-VAE on a simulated tabular credit dataset. The simulated data has 20000 observations which are generated using several underlying factors represented by 11 variables:

1. Two demographic variables: Variable L for gender, and variable M for race.
2. Four Utilization variables named Ub, Ub_1, Ub_2, Ub_3 .
3. Four Debt stress variables S, S_1, S_2, S_3 and debt stress variable threshold T .

These 11 factors induces a credit tabular dataset with 19 features:

1. Mortgage, Utilization, Amount Past Due
2. Four balance features with different periods: Balance
3. Four credit inquiry features
4. Four open trade features
5. Four delinquency status features

Data processing. To improve performances across 3 VAE models, we perform several pre-processing steps consisting of log transform and normalization. Particularly, prior to training the model, we apply log transform on continuous variables of the original dataset, and apply min-max normalization on both continuous and categorical variables. Once the models are trained and the synthetic data is generated, we perform post-processing steps including: clipping the generated data to range $[0,1]$, de-normalizing categorical variables and rounding off to the nearest integer, and de-logging and de-normalizing continuous variables.

6.3 Evaluation metrics

The synthetic tabular data is assessed on two aspects: Classifier 2-sample test (C2ST) or Detection test and statistical similarity. The first metric, proposed by Zhao et al. (2021), evaluates the faithfulness of the synthetic data to the original data. Unlike ML-efficacy, which measures the (test) performance gap between predictive models trained on real versus synthetic data, C2ST evaluates the ability of a discriminant classifier to detect real data from fake data. Combined with statistical similarity, these metrics thus quantify the realism of the synthetic data set and whether it can be used as a proxy for the original data.

6.3.1 Statistical Similarity

We use two metrics to measure the statistical similarity between the artificial and original datasets.

Jensen-Shannon divergence (JSD) (Nielsen (2019)). The JSD, a symmetric version of KL divergence, calculates the relative entropy in information represented by distributions between individual features of real versus fake data. The metric is applied to the (normalized) synthetic and real data, and is bounded between 0 and 1. To allow easy interpretation, we provide the averaged JSD across all features as the final measure.

Correlation Difference (CD). We use CD to capture how well the feature relations are maintained in the synthetic data. To calculate CD, we first calculate the pairwise correlation matrices for real and synthetic data separately. The final CD is the difference between these two correlation matrices calculated using Frobenious norm. We remark that for each correlation matrix, three cases are considered: (1) correlation between two continuous features is measured via Pearson correlation coefficient, (2) correlation between two categorical features is measured using Theil uncertainty coefficient, and (3) correlation between categorical and continuous features is measured with correlation ratio.

6.3.2 Detection Test/Classifier 2-sample test (C2ST)

The original and the generated data should be indistinguishable not only from a statistical viewpoint but also from a machine-learning viewpoint. This is important for downstream tasks such as fraud

detection because we don't want the fraud classifiers to make a distinction between real and generated data, leading to a possibility that the classifiers flag the generated data as fraud.

Thus, to evaluate how closely the synthetic data follows the real data, we perform the Classifier 2-sample test (C2ST). The evaluation process consists of the following steps: (1) Split the original data into two datasets D_{train} and D_{test} , (2) Use D_{train} to train the generative models and generate a fake data set D_{syn} with the same size as D_{test} , (3) Create a new dataset \mathcal{T} with D_{test} (labeled 1) and D_{syn} (labeled 0) for real and fake data respectively, (4) Split \mathcal{T} into \mathcal{T}_{train} and \mathcal{T}_{test} , and train a binary classifier on \mathcal{T}_{train} to produce the probability of a datapoint being fake, (5) Use *Area Under the ROC Curve (AUC)* to measure the performance of this classifier on test data \mathcal{T}_{test} .

6.4 Results analysis

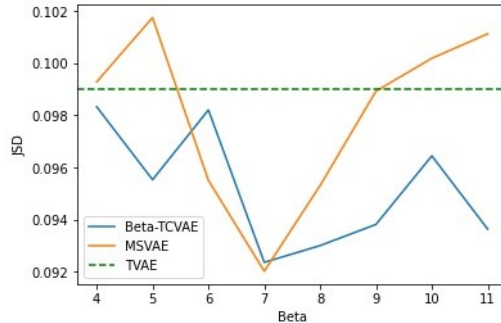
In this section, we present the empirical results evaluating the synthetic credit data generated by our main method MS-VAE. This process computes the metrics specified in Section 6.3, and the results are compared with two benchmark models: TVAE and β -TCVAE. Across three models, we perform hyper-parameters tuning for latent dimension and β values. Specifically, each model was trained for 3000 epochs, with latent dimensions ranging from 2 to 14, and β values ranging from 2 to 9.

The tuning results are included in Figure 6. The graph shows that MS-VAE generates synthetic data with the highest JSD at $\beta = 7$ and latent 9. In the following parts, we provide experimental results across three VAE models at these specified hyper-parameters.

Statistical similarity. Results on JSD and CD performance for MS-VAE and benchmark models are presented in Table 1. Here, we can see that while MS-VAE outperforms benchmark models on JSD, CD metric indicates that β -TCVAE best preserves the features interactions. This is perhaps due to its focus on latent disentanglement, while MS-VAE has a balance between reconstruction quality and disentanglement outcomes. The JSD performance comparison for each individual feature of the three models are provided in Appendix N.

Detection Test (C2ST). We follow the steps detailed in Section 6.3.2 to perform Detection Test for MS-VAE's generated data. Two binary classifiers used are Logistic Regression and Random Forest. To make the task more challenging, we also include the strongest-performing classifier from our experiments: XGBoost. As shown in Table 2, MS-VAE outperforms the other two benchmarks on C2ST metric. We remark that an AUC of 0.5 means that the fake data is indistinguishable from the original data. Thus, XGBoost having AUC of 0.738 when detecting fake data implies that the MS-VAE-generated synthetic data is relatively faithful and similar (average JSD = 0.071) to the original dataset. We want to remark that an AUC of 0.7 corresponds to a very good performance as indicated in Zein & Urvoy (2022). β -TCVAE, while having better CD performance, has the worst performance among the 3 models in this test. This suggests that β -TCVAE's relatively lower reconstruction quality makes it vulnerable to fake data classifiers.

Figure 6: JSD results for different β at latent dim = 9



6.5 Further discussions

In this section, we provide several examples of the individual feature performance of synthetic data generated by MS-VAE, β -TCVAE, and TVAE and their corresponding analyses. The four types of

Table 1: Statistical Similarity performance for latent dim = 9, $\beta = 7$

Models/Metrics	JSD ↓		CD ↓	
	Train	Test	Train	Test
β -TCVAE	0.068	0.0923	0.855	0.926
MS-VAE	0.071	0.092	0.868	0.99
TVAE	0.066	0.099	1.259	1.183

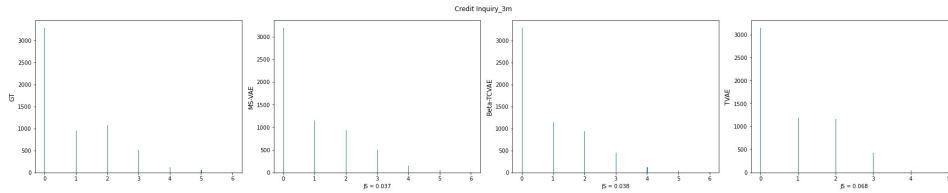
Table 2: Detection Test (C2ST) performance for latent dim = 9, $\beta = 7$

Models/AUC ↓	XGBoost		Logistic Regression		Random Forest	
	Train	Test	Train	Test	Train	Test
β -TCVAE	0.826	0.81	0.588	0.595	0.8	0.809
MS-VAE	0.74	0.738	0.581	0.592	0.749	0.741
TVAE	0.745	0.743	0.557	0.577	0.754	0.75

variables discussed below are relatively representative of the attributes available within the original credit tabular dataset.

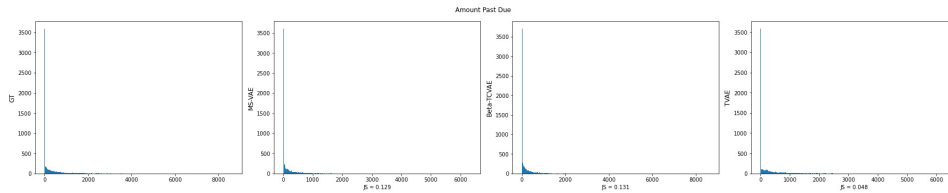
Discrete variables. The categorical (discrete) feature **Credit Inquiry_3m** has 7 possible values. Figure 8 shows the distribution plot of the original distribution for this feature against the distribution of the generated data produced by 3 VAE models. All models do very well in terms of reproducing the density for the most frequent value (value 0). Overall all three models do well in this case. However, there is a slight mismatch for the densities of values 1 and 2. Even though in original data, value 1 occurs less frequently than 2, both MS-VAE and β -TCVAE couldn't capture this property. TVAE even misses the underrepresented value 6. Hence, additional care is required to handle the class imbalance problem for categorical features.

Figure 7: Original data distribution (1st plot) vs distribution for generated data from MS-VAE (2nd plot), β -TCVAE (3rd plot), and TVAE (4th plot) for column **Credit Inquiry_3m**



Mixed data type variables. The Amount Past Due feature contains both categorical value (denoted by 0) and continuous values. For this special mixed-data type distribution, MS-VAE reconstructs the original data sufficiently well. On the other hand, β -TCVAE produces a somewhat over-concentrated histogram, while continuous values generated by TVAE are too spread out. From Figure 8, we observe that TVAE indicates a lack of special treatment to handle this feature type, while the distortion from β -TCVAE might come from its large reconstruction error when compared to MS-VAE.

Figure 8: Original data distribution (1st plot) vs distribution for generated data from MS-VAE (2nd plot), β -TCVAE (3rd plot), and TVAE (4th plot) for column **Amount Past Due**



Skewed continuous variables. **Balance_6m** and **Mortgage** are two features with skewed distribution. Even though their general distribution shapes are not widely different, the result is quite surprising.

For **Balance_6m**, all models capture the original data sufficiently well, while for **Mortgage**, only MS-VAE provides a decent performance(See Figure 9 and 10). A possible explanation for this phenomenon is the non-trivial irregularity appearing in **Mortgage** feature (with a small abrupt peak in the middle).

Figure 9: Original data distribution (1st plot) vs distribution for generated data from MS-VAE (2nd plot), β -TCVAE (3rd plot), and TVAE (4th plot) for column **Balance_6m**

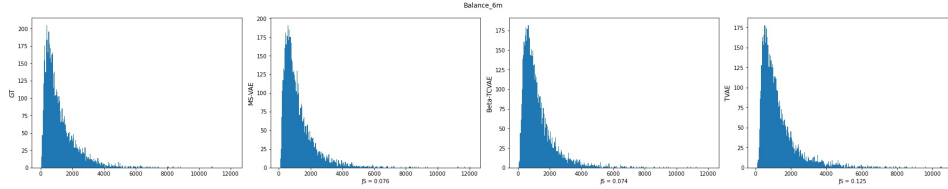
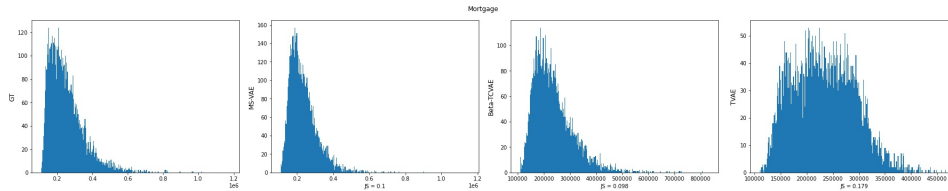
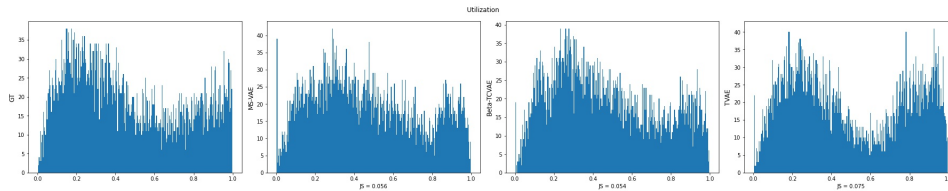


Figure 10: Original data distribution (1st plot) vs distribution for generated data from MS-VAE (2nd plot), β -TCVAE (3rd plot), and TVAE (4th plot) for column **Mortgage**



Multi-mode continuous variables. **Utilization** is a feature with multi-mode distribution. From Figure 11, β -TCVAE performs best among all models for this type of distribution. On the other hand, MS-VAE produces unwanted artifacts at the left end, while TVAE’s reconstructed distribution is more noisy than expected. For complex distributions as in this case, further research is needed to produce improvement.

Figure 11: Original data distribution (1st plot) vs distribution for generated data from MS-VAE (2nd plot), β -TCVAE (3rd plot), and TVAE (4th plot) for column **Utilization**



7 Model interpretability

Interpretability of latent space is especially important in finance. If we want to train a financial machine learning model using the data generated by VAE models, we need to explain clearly what are the sources (or the latent variables) used for the data generation process, and describe the generation process in details. Taking a vector of real numbers and then feeding into the black-box decoder as in a traditional VAE certainly doesn’t offer enough interpretability for compliance and regulation purposes.

7.1 Correlation of latent variables and original data

One advantage of β -TCVAE and MS-VAE over TVAE is that they allow the disentanglement of variables of latent space thanks to the total correlation penalty term. From the disentanglement, we can hope to associate individual coordinate of the latent variables to the underlying factors from which the input distribution can be recovered. To check the effectiveness of this disentanglement with

Table 3: Correlation between coordinates of latent vectors produced by different models and the original input features. We only include correlations that is significant (higher than 0.75).

Coordinate type	β -TCVAE latent correlation with input (Stage one of MS-VAE)	TVAE latent correlation with input
z_1	No significant correlation	No significant correlation
z_2	Mortgage 0.910502	No significant correlation
z_4	Credit Inquiry_12m 0.898419 Open Trade_12m 0.890393	No significant correlation
z_5	Credit Inquiry_6m 0.808494 Open Trade_6m 0.832294	No significant correlation
z_6	Utilization 0.904766 Balance 0.879174	No significant correlation
z_7	Balance_3m 0.758381 Balance_6m 0.849974 Balance_12m 0.851672	No significant correlation
z_9	Delinquency Status 0.725198 Delinquency Status_3m 0.877644 Delinquency Status_6m 0.930754 Delinquency Status_12m 0.928545	No significant correlation

the end goal of recovering the hidden underlying factors, we measure the correlation between the model latent space’s individual coordinate and the features of the original data. For our setting with 9-dimensional latent space, for each coordinate z_1, \dots, z_9 , we look at its correlations with each of the 19 original input features from tabular data. We define a correlation as **significant** if its value is at least 0.75. We only retain significant correlations for each coordinate. Table 3 shows the correlations for 2 models β -TCVAE and *TVAE*. We note that as the performance of β -TCVAE in Table 3 is precisely the first stage of our multi-stage model, it carries the main interpretability information for MS-VAE.

From the correlation table, we observe that for β -TCVAE model, each latent variable clearly corresponds to a separate group of features in the original data. More specifically, z_2 corresponds to the mortgage feature, while z_4 and z_5 variables are correlated to credit inquiry and open trade features for two separate periods 12 months and 6 months. On the other hand, z_9 is mainly correlated to delinquency status variables. Finally, z_6 corresponds to **Utilization** and **Balance** variables, while z_7 is correlated to the group of remaining 3 balance variables with different recent month periods. Each of these separate groups depends on a separate subset of underlying factors, suggesting that β -TCVAE did a reasonable job in separating the underlying factors. However, as the latent dimension is less than the input dimension and the group of input features may all depend on a single factor, it is very challenging to ask the model to separate entirely all features (each coordinate only has a significant relation with one feature).

Meanwhile, correlations for TVAe latent space’s coordinates are relatively insignificant and spread out over all input features. A more detailed table without the 0.75 threshold is provided in the Appendix N Table 7.

7.2 Effect of individual latent coordinate perturbation on generated data

To visually estimate the effect of disentangled representation of the latent space for β -TCVAE and MS-VAE, we perturb a fixed coordinate of the latent vectors by a reasonably large margin. We then investigate the changes within the column features and compare with the changes produced by TVAe model under the same perturbation. Figure 12 shows the plot of the reconstructed data from different models when the corresponding latent vector’s 2^{nd} coordinate is altered. Modifying the latent vector of β -TCVAE in the 2^{nd} coordinate only affects the feature **Mortgage** widely, while keeping the **Utilization**’s distribution nearly the same. This suggests a possible one-to-one relation between the latent vector’s 2^{nd} coordinate and the **Mortgage** feature. In other words, the 2^{nd} coordinate seems to

be a factor that dictates the **Mortgage** feature. Their correlation shown in Table 3 further solidifies this hypothesis.

Varying the second component of the correlated factor Z in the MS-VAE’s second stage kept **Mortgage** and **Utilization** almost intact. The factors controlling these two features are thus learned via β -TCVAE in the first stage. As the core learning is done in the first stage, the factor Z will additionally improve the reconstruction by taking into account other features that haven’t been captured well in the first stage.

On the other hand, changing the latent variable from TVAE model has a slight impact on both features **Mortgage** and **Utilization**, but there seems to be no strong relation between these variables. This contrast indicates that β -TCVAE (first stage of MS-VAE) can potentially separate and recover distinct, informative factors of variations from credit data distribution, while TVAE does not achieve this effect.

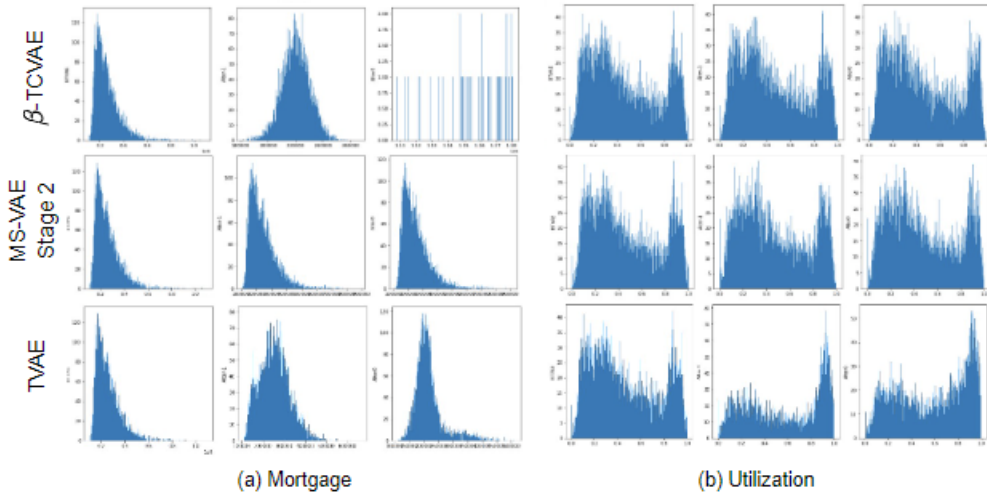


Figure 12: Effect of perturbation of the second coordinate of latent vectors on generated data. The left panel is for **Mortgage** feature, and the right is for **Utilization** feature. For each panel, in the first row, we perturb the second coordinate of the latent vector from β -TCVAE model. The second row is for the correlated latent factor Z learned in the second stage of MS-VAE (from residual between original data and constructed data in stage one), and the third is for TVAE. In each panel, the first column is the original reconstruction data. In the second and third columns, we replace the second coordinate of the latent vector by zero vector and by constant vector v_5 respectively. Here v_5 is the vector with all entries equal 5.

8 Conclusion

In this work, we proposed a novel graphical model for DR learning that, by virtue of being D-separated, overcomes the trade-off between reconstruction and disentanglement. To implement this graphical model, we introduced a multi-stage deep generative model, MS-VAE, that learns the independent and correlated latent variables in two separate stages of training. We showed that this model dramatically improves the reconstruction of preexisting DR learning methods while maintaining the same level of disentanglement. Furthermore, our experiments for MS-GAN and MS-FLOW (Appendices F and E, respectively) demonstrated that our framework is agnostic to both the level of supervision (e.g. unsupervised, weakly supervised, fully supervised) and to the underlying model (e.g. VAEs, GANs, normalizing flows).

We have implemented the multi-stage model for generating synthetic credit tabular datasets as well. Compared to other leading benchmark models, MS-VAE maintains a harmonious balance between providing high-quality data and ease of understanding. The clarity regarding latent space features it provides is crucial for applications where transparent decision-making is key. In summary, this innovative model marks a notable advancement in simulating synthetic tabular data, merging enhanced performance with transparent interpretability.

While MS-VAE’s two stage training is effective in alleviating the trade-off between learning disentangled representations and reconstruction quality in existing DR learning methods, in future, we aim to develop a single coherent DR model that does not require two separate training steps.

References

- Abadi, M., Barham, P., Chen, J., Chen, Z., Davis, A., Dean, J., Devin, M., Ghemawat, S., Irving, G., Isard, M., et al. Tensorflow: A system for large-scale machine learning. In *12th {USENIX} Symposium on Operating Systems Design and Implementation ({OSDI} 16)*, pp. 265–283, 2016.
- Aubry, M., Maturana, D., Efros, A. A., Russell, B. C., and Sivic, J. Seeing 3d chairs: exemplar part-based 2d-3d alignment using a large dataset of cad models. In *Proceedings of the IEEE conference on computer vision and pattern recognition*, pp. 3762–3769, 2014.
- Bengio, Y., Courville, A., and Vincent, P. Representation learning: A review and new perspectives. *IEEE transactions on pattern analysis and machine intelligence*, 35(8):1798–1828, 2013.
- Chang, A. X., Funkhouser, T., Guibas, L., Hanrahan, P., Huang, Q., Li, Z., Savarese, S., Savva, M., Song, S., Su, H., et al. Shapenet: An information-rich 3d model repository. *arXiv preprint arXiv:1512.03012*, 2015.
- Chen, T. Q., Li, X., Grosse, R. B., and Duvenaud, D. K. Isolating sources of disentanglement in variational autoencoders. In *Advances in Neural Information Processing Systems*, pp. 2610–2620, 2018.
- Chen, X., Duan, Y., Houthoofd, R., Schulman, J., Sutskever, I., and Abbeel, P. Infogan: Interpretable representation learning by information maximizing generative adversarial nets. In *Advances in neural information processing systems*, pp. 2172–2180, 2016.
- Choi, E., Biswal, S., Malin, B. A., Duke, J., Stewart, W. F., and Sun, J. Generating multi-label discrete patient records using generative adversarial networks. In *Proceedings of the Machine Learning for Health Care Conference, MLHC 2017, Boston, Massachusetts, USA, 18-19 August 2017*, volume 68 of *Proceedings of Machine Learning Research*, pp. 286–305. PMLR, 2017. URL <http://proceedings.mlr.press/v68/choi17a.html>.
- Deng, L. The mnist database of handwritten digit images for machine learning research [best of the web]. *IEEE Signal Processing Magazine*, 29(6):141–142, 2012.
- Dinh, L., Krueger, D., and Bengio, Y. Nice: Non-linear independent components estimation. *CoRR*, 2014. URL <http://arxiv.org/abs/1410.8516v6>.
- Dinh, L., Sohl-Dickstein, J., and Bengio, S. Density estimation using real nvp. *arXiv preprint arXiv:1605.08803*, 2016.
- Dumoulin, V., Perez, E., Schucher, N., Strub, F., Vries, H. d., Courville, A., and Bengio, Y. Feature-wise transformations. *Distill*, 3(7):e11, 2018.
- Durkan, C., Bekasov, A., Murray, I., and Papamakarios, G. Neural spline flows. *CoRR*, 2019. URL <http://arxiv.org/abs/1906.04032v1>.
- Egger, B., Schönborn, S., Schneider, A., Kortylewski, A., Morel-Forster, A., Blumer, C., and Vetter, T. Occlusion-aware 3d morphable models and an illumination prior for face image analysis. *IJCV*, 2018.
- Gerig, T., Morel-Forster, A., Blumer, C., Egger, B., Lüthi, M., Schönborn, S., and Vetter, T. Morphable face models - an open framework. In *FG*, pp. 75–82, 2018.
- Goodfellow, I. J., Pouget-Abadie, J., Mirza, M., Xu, B., Warde-Farley, D., Ozair, S., Courville, A. C., and Bengio, Y. Generative adversarial nets. In *Neural Information Processing Systems*, 2014.
- Heusel, M., Ramsauer, H., Unterthiner, T., Nessler, B., and Hochreiter, S. GANS trained by a two time-scale update rule converge to a local nash equilibrium. In *Neural Information Processing Systems*, 2017.

- Higgins, I., Matthey, L., Pal, A., Burgess, C., Glorot, X., Botvinick, M., Mohamed, S., and Lerchner, A. beta-vae: Learning basic visual concepts with a constrained variational framework. *ICLR*, 2(5): 6, 2017.
- Hu, Q., Szabó, A., Portenier, T., Favaro, P., and Zwicker, M. Disentangling factors of variation by mixing them. In *2018 IEEE Conference on Computer Vision and Pattern Recognition, CVPR 2018, Salt Lake City, UT, USA, June 18-22, 2018*, pp. 3399–3407. IEEE Computer Society, 2018. doi: 10.1109/CVPR.2018.00358. URL http://openaccess.thecvf.com/content_cvpr_2018/html/Hu_Disentangling_Factors_of_CVPR_2018_paper.html.
- Huang, C.-W., Krueger, D., Lacoste, A., and Courville, A. Neural autoregressive flows. *CoRR*, 2018. URL <http://arxiv.org/abs/1804.00779v1>.
- Huang, X. and Belongie, S. Arbitrary style transfer in real-time with adaptive instance normalization. In *Proceedings of the IEEE International Conference on Computer Vision*, pp. 1501–1510, 2017.
- Isola, P., Zhu, J.-Y., Zhou, T., and Efros, A. A. Image-to-image translation with conditional adversarial networks. In *Proceedings of the IEEE conference on computer vision and pattern recognition*, pp. 1125–1134, 2017.
- Jeong, Y. and Song, H. O. Learning discrete and continuous factors of data via alternating disentanglement. *arXiv preprint arXiv:1905.09432*, 2019.
- Kim, H. and Mnih, A. Disentangling by factorising. *arXiv preprint arXiv:1802.05983*, 2018.
- Kingma, D. P. and Welling, M. Auto-encoding variational bayes. In *2nd International Conference on Learning Representations, ICLR, 2014*.
- Kortylewski, A., Egger, B., Schneider, A., Gerig, T., Morel-Forster, A., and Vetter, T. Analyzing and reducing the damage of dataset bias to face recognition with synthetic data. In *CVPRW*, 2019.
- Kumar, A., Sattigeri, P., and Balakrishnan, A. Variational inference of disentangled latent concepts from unlabeled observations. *arXiv preprint arXiv:1711.00848*, 2017.
- Lake, B. M., Ullman, T. D., Tenenbaum, J. B., and Gershman, S. J. Building machines that learn and think like people. *Behavioral and brain sciences*, 40, 2017.
- Lample, G., Zeghidour, N., Usunier, N., Bordes, A., Denoyer, L., and Ranzato, M. Fader networks: Manipulating images by sliding attributes. In Guyon, I., von Luxburg, U., Bengio, S., Wallach, H. M., Fergus, R., Vishwanathan, S. V. N., and Garnett, R. (eds.), *Advances in Neural Information Processing Systems 30: Annual Conference on Neural Information Processing Systems 2017, 4-9 December 2017, Long Beach, CA, USA*, pp. 5967–5976, 2017. URL <http://papers.nips.cc/paper/7178-fader-networksmanipulating-images-by-sliding-attributes>.
- LeCun, Y., Huang, F. J., and Bottou, L. Learning methods for generic object recognition with invariance to pose and lighting. In *Proceedings of the 2004 IEEE Computer Society Conference on Computer Vision and Pattern Recognition, 2004. CVPR 2004.*, volume 2, pp. II–104. IEEE, 2004.
- LeCun, Y., Bengio, Y., and Hinton, G. Deep learning. *nature*, 521(7553):436, 2015.
- Lee, W., Kim, D., Hong, S., and Lee, H. High-fidelity synthesis with disentangled representation. In *European Conference on Computer Vision*, pp. 157–174. Springer, 2020.
- Lezama, J. Overcoming the disentanglement vs reconstruction trade-off via jacobian supervision. 2018.
- Liu, Z., Luo, P., Wang, X., and Tang, X. Large-scale celebfaces attributes (celeba) dataset.
- Liu, Z., Luo, P., Wang, X., and Tang, X. Deep learning face attributes in the wild. In *Proceedings of International Conference on Computer Vision (ICCV)*, December 2015.
- Locatello, F., Bauer, S., Lucic, M., Gelly, S., Schölkopf, B., and Bachem, O. Challenging common assumptions in the unsupervised learning of disentangled representations. *arXiv preprint arXiv:1811.12359*, 2018.

- Mathieu, M. F., Zhao, J. J., Zhao, J., Ramesh, A., Sprechmann, P., and LeCun, Y. Disentangling factors of variation in deep representation using adversarial training. In *Advances in Neural Information Processing Systems*, pp. 5040–5048, 2016.
- Mirza, M. and Osindero, S. Conditional generative adversarial nets. *arXiv preprint arXiv:1411.1784*, 2014.
- Nielsen, F. On the jensen–shannon symmetrization of distances relying on abstract means. *Entropy*, 21(5), 2019. ISSN 1099-4300. URL <https://www.mdpi.com/1099-4300/21/5/485>.
- Perarnau, G., van de Weijer, J., Raducanu, B., and Álvarez, J. M. Invertible conditional gans for image editing. *CoRR*, abs/1611.06355, 2016. URL <http://arxiv.org/abs/1611.06355>.
- Perez, E., Strub, F., De Vries, H., Dumoulin, V., and Courville, A. Film: Visual reasoning with a general conditioning layer. *arXiv preprint arXiv:1709.07871*, 2017.
- Perez, E., Strub, F., De Vries, H., Dumoulin, V., and Courville, A. Film: Visual reasoning with a general conditioning layer. In *Thirty-Second AAAI Conference on Artificial Intelligence*, 2018.
- Radford, A., Metz, L., and Chintala, S. Unsupervised representation learning with deep convolutional generative adversarial networks. *arXiv preprint arXiv:1511.06434*, 2015.
- Razavi, A., van den Oord, A., and Vinyals, O. Generating diverse high-fidelity images with vq-vae-2. In *Advances in Neural Information Processing Systems*, pp. 14837–14847, 2019.
- Reed, S. E., Zhang, Y., Zhang, Y., and Lee, H. Deep visual analogy-making. In *Advances in neural information processing systems*, pp. 1252–1260, 2015.
- Reed, S. E., Akata, Z., Yan, X., Logeswaran, L., Schiele, B., and Lee, H. Generative adversarial text to image synthesis. In Balcan, M. and Weinberger, K. Q. (eds.), *Proceedings of the 33rd International Conference on Machine Learning, ICML 2016, New York City, NY, USA, June 19-24, 2016*, volume 48 of *JMLR Workshop and Conference Proceedings*, pp. 1060–1069. JMLR.org, 2016. URL <http://proceedings.mlr.press/v48/reed16.html>.
- Rezende, D. J., Mohamed, S., and Wierstra, D. Stochastic backpropagation and approximate inference in deep generative models. *arXiv preprint arXiv:1401.4082*, 2014.
- Srivastava, A., Valkov, L., Russell, C., Gutmann, M. U., and Sutton, C. Veegan: Reducing mode collapse in gans using implicit variational learning. In *Advances in Neural Information Processing Systems*, pp. 3308–3318, 2017.
- Sugiyama, M., Suzuki, T., and Kanamori, T. *Density ratio estimation in machine learning*. Cambridge University Press, 2012.
- Szabó, A., Hu, Q., Portenier, T., Zwicker, M., and Favaro, P. Challenges in disentangling independent factors of variation. In *6th International Conference on Learning Representations, ICLR 2018, Vancouver, BC, Canada, April 30 - May 3, 2018, Workshop Track Proceedings*. OpenReview.net, 2018. URL <https://openreview.net/forum?id=B1e7-DsIf>.
- Ulyanov, D., Vedaldi, A., and Lempitsky, V. Instance normalization: The missing ingredient for fast stylization. *arXiv preprint arXiv:1607.08022*, 2016.
- van Steenkiste, S., Locatello, F., Schmidhuber, J., and Bachem, O. Are disentangled representations helpful for abstract visual reasoning? In *Advances in Neural Information Processing Systems*, pp. 14222–14235, 2019.
- Wang, Z., Simoncelli, E. P., and Bovik, A. C. Multiscale structural similarity for image quality assessment. In *The Thrity-Seventh Asilomar Conference on Signals, Systems & Computers, 2003*, volume 2, pp. 1398–1402. Ieee, 2003.
- Wang, Z., Bovik, A. C., Sheikh, H. R., and Simoncelli, E. P. Image quality assessment: from error visibility to structural similarity. *IEEE transactions on image processing*, 13(4):600–612, 2004.
- Xu, L., Skoularidou, M., Cuesta-Infante, A., and Veeramachaneni, K. *Modeling Tabular Data Using Conditional GAN*. Curran Associates Inc., Red Hook, NY, USA, 2019.

Yahi, A., Vanguri, R., Elhadad, N., and Tatonetti, N. P. Generative adversarial networks for electronic health records: A framework for exploring and evaluating methods for predicting drug-induced laboratory test trajectories. *CoRR*, abs/1712.00164, 2017. URL <http://arxiv.org/abs/1712.00164>.

Zein, E. H. and Urvoy, T. Tabular data generation: Can we fool XGBoost? In *NeurIPS 2022 First Table Representation Workshop*, 2022. URL <https://openreview.net/forum?id=tTQzJ6TJGVi>.

Zhang, H., Xu, T., Li, H., Zhang, S., Huang, X., Wang, X., and Metaxas, D. N. Stackgan: Text to photo-realistic image synthesis with stacked generative adversarial networks. *CoRR*, abs/1612.03242, 2016. URL <http://arxiv.org/abs/1612.03242>.

Zhao, Z., Kumar, A., Birke, R., and Chen, L. Y. Ctab-gan: Effective table data synthesizing. In Balasubramanian, V. N. and Tsang, I. (eds.), *Proceedings of The 13th Asian Conference on Machine Learning*, volume 157 of *Proceedings of Machine Learning Research*, pp. 97–112. PMLR, 17–19 Nov 2021. URL <https://proceedings.mlr.press/v157/zhao21a.html>.

1. For all authors...
 - (a) Do the main claims made in the abstract and introduction accurately reflect the paper’s contributions and scope? [Yes]
 - (b) Did you describe the limitations of your work? [Yes]
 - (c) Did you discuss any potential negative societal impacts of your work? [Yes]
 - (d) Have you read the ethics review guidelines and ensured that your paper conforms to them? [Yes]
2. If you are including theoretical results...
 - (a) Did you state the full set of assumptions of all theoretical results? [N/A]
 - (b) Did you include complete proofs of all theoretical results? [N/A]
3. If you ran experiments...
 - (a) Did you include the code, data, and instructions needed to reproduce the main experimental results (either in the supplemental material or as a URL)? [Yes]
 - (b) Did you specify all the training details (e.g., data splits, hyperparameters, how they were chosen)? [Yes]
 - (c) Did you report error bars (e.g., with respect to the random seed after running experiments multiple times)? [Yes]
 - (d) Did you include the total amount of compute and the type of resources used (e.g., type of GPUs, internal cluster, or cloud provider)? [N/A]
4. If you are using existing assets (e.g., code, data, models) or curating/releasing new assets...
 - (a) If your work uses existing assets, did you cite the creators? [Yes]
 - (b) Did you mention the license of the assets? [N/A]
 - (c) Did you include any new assets either in the supplemental material or as a URL? [Yes]
 - (d) Did you discuss whether and how consent was obtained from people whose data you’re using/curating? [N/A]
 - (e) Did you discuss whether the data you are using/curating contains personally identifiable information or offensive content? [N/A]
5. If you used crowdsourcing or conducted research with human subjects...
 - (a) Did you include the full text of instructions given to participants and screenshots, if applicable? [N/A]
 - (b) Did you describe any potential participant risks, with links to Institutional Review Board (IRB) approvals, if applicable? [N/A]
 - (c) Did you include the estimated hourly wage paid to participants and the total amount spent on participant compensation? [N/A]

A Traversal Results: Figures

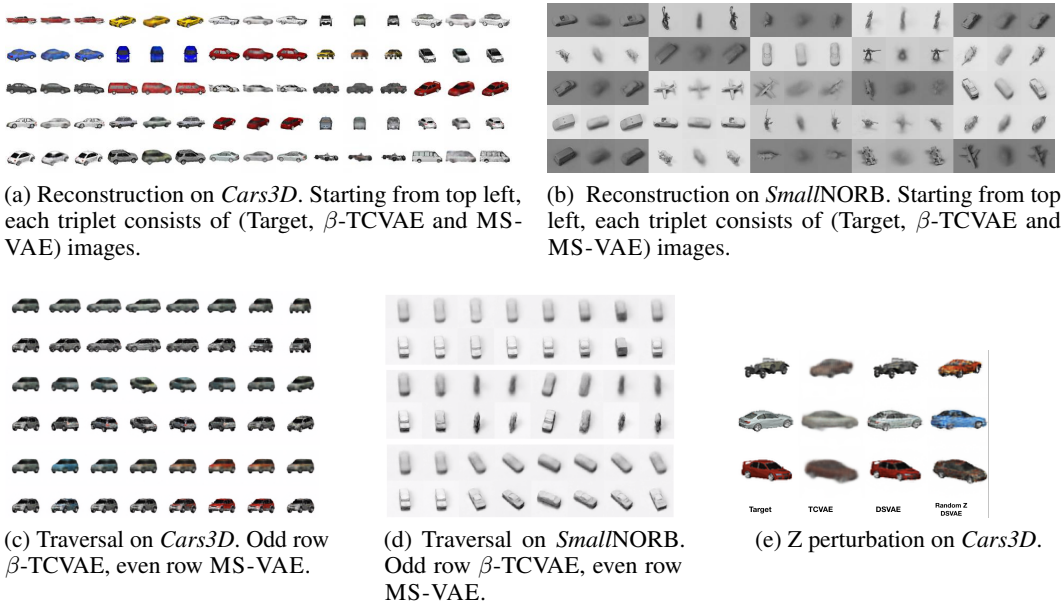


Figure 13: Qualitative results on the *Cars3D* and *SmallNORB* datasets for β -TCVAE and MS-VAE.

B Choosing C and Z

We study the impact of the dimensionality of C and Z on the reported results in this section. To do so, we fix a value of β and sweep over multiple values for C and Z .

Choosing C : For C , we sweep over the range $[1 - 10, 20, 50]$ for both the datasets. Figure 14a and 14b show the MIG and ELBO for the same. We can see that $|C| = 10$ achieves a good combination of MIG and ELBO for the *Cars3D* dataset. While there is high variance in the MIG for *SmallNORB*, $|C| = 10$ performs reasonably well. This is also consistent with the large scale study in (Locatello et al., 2018), which suggests that a value of 10 for the dimensionality of C is optimal for DR learning.

Choosing Z : Similarly for Z , we sweep over a set of candidate values $[5, 10, 50, 90]$ and evaluate the FID and MIG. For evaluating the FID, we consider both reconstructions (by sampling Z from the posterior) and 'Random Z ' (by sampling a random Z from the prior). We also look at the MI H. We find smaller values, 5 and 10 for *Cars3D* and *SmallNORB*, respectively, achieve a good combination of all the three quantities of interest. The results are shown in ??.

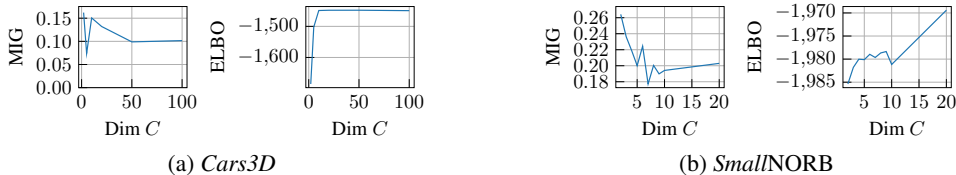


Figure 14: MIG and ELBO for different dimensionality of C for *Cars3D* and *SmallNORB* at $\beta = 4$

Qualitatively, Figure 16 and Figure 17 show the effect of varying the dimensionality of C and Z . For a small C (Figure 16), the underlying disentanglement method does a poor job at disentangling the meaningful latent variables, which further results in blurry images. In this case, Z has substantial control over the image—it adds various missing details to Y such as color. In contrast, Figure 17 shows traversals for a high value of C . Now, each individual dimension of C controls fewer

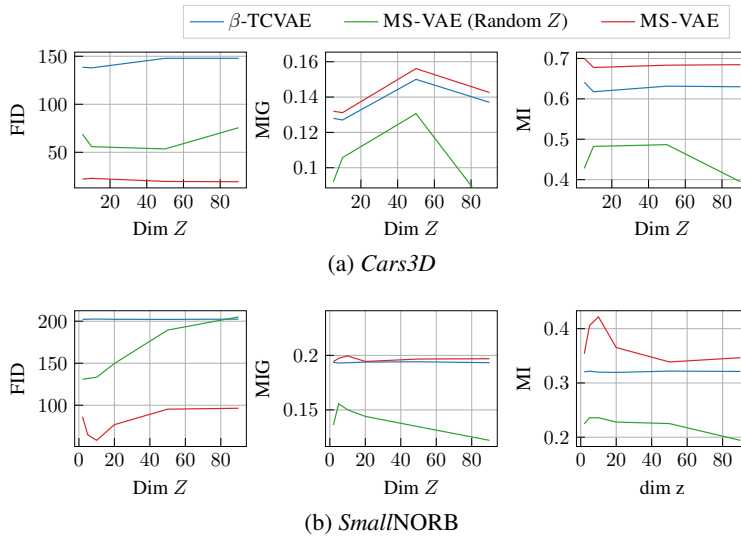


Figure 15: MIG, FID and MI plots for MS-VAE as a function of the dimensionality of Z for *Cars3D* and *SmallNORB* ($\beta = 4$).

independent factors, the Y images are relatively sharper, and adding Z improves them further. Similar conclusions hold for *SmallNORB* as shown in Fig. 19 and 18.



Figure 16: Traversals for cars for small C ($c = 2$, $z = 8$ and $\beta = 4$). Odd rows β -TCVAE and even rows MS-VAE. We can see the Y images are blurry and various factors are entangled.



Figure 17: Traversals for cars large C ($c = 10$, $z = 5$ and $\beta = 4$). Odd rows β -TCVAE and even rows MS-VAE. Larger C achieves greater disentanglement and Z further refines the images.

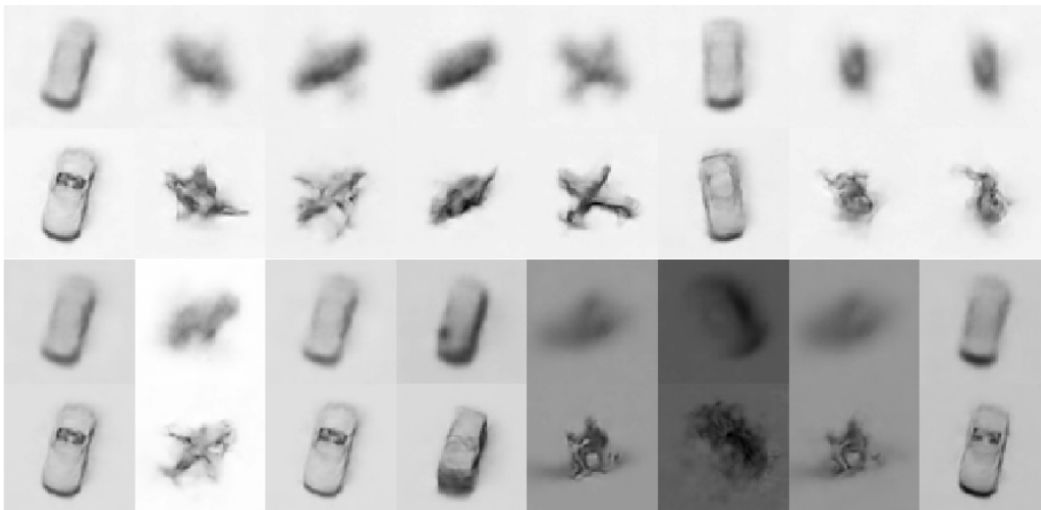


Figure 18: Traversals for SmallNORB $c = 2$, $z = 8$ and $\beta = 4$. Odd rows β -TCVAE and even rows MS-VAE.

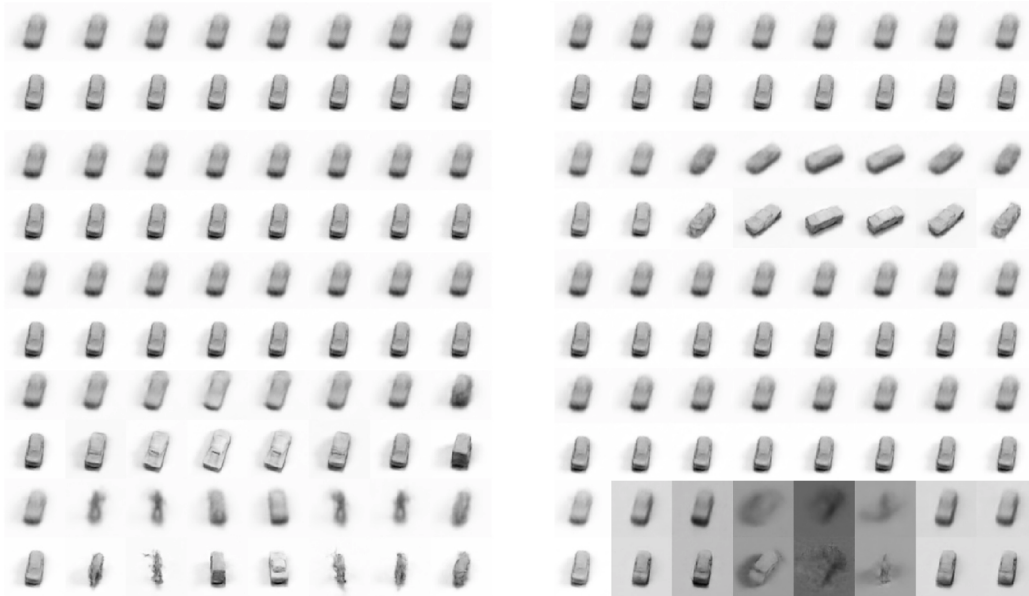


Figure 19: Traversals for SmallNORB $c = 10$, $z = 10$ and $\beta = 6$. Odd rows β -TCVAE and even rows MS-VAE.

C CelebA Results

Please see Figure 20 and Figure 21.

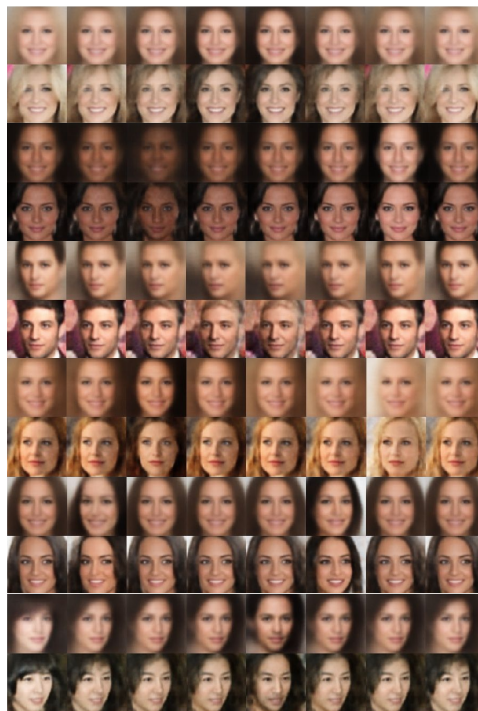


Figure 20: CelebA Latent traversal on C . Odd rows are β -TCVAE and even rows are MS-VAE.



Figure 21: CelebA Reconstruction plots.

D MS-VAE for Simple Pendulum

A simple, 2D pendulum is comprised of a bob with mass m attached to a string of length L where the mass of the string is negligible in comparison to m . The primary forces acting upon the bob are the gravitational force, the tension force of the string, and the damping force from air resistance. Let θ be the angular displacement of the weight (the corresponding angle with respect to the y-direction). The pendulum’s motion can be completely described as $\frac{d^2\theta}{dt^2} = -\frac{b}{m} \frac{d\theta}{dt} - \frac{g}{L} \sin \theta$, where b is the damping coefficient and g is the gravitational acceleration constant (the initial angular displacement/velocity are constant).

In this toy example, we assume that, given the length L , the damping coefficient B , and the mass M , the angular displacement of a pendulum is generated by a noiseless simulator $S : (L, M, B) \rightarrow \theta$ where $\theta := \{\theta_0, \theta_1, \dots, \theta_T\}$, $\theta_i \in [-\pi, \pi]$, and $T = 100$. Using samples from S where only L and B are known a priori, we aim to learn a hierarchical, generative model for the pendulum where *all generative factors are completely disentangled*. With MS-VAE, we can achieve this by learning the graphical model in Figure 22. We define Y_0 as the undamped angular displacement and Y_1 as the damped angular displacement with fixed mass ($M = 1$).

We train our model in three separate steps. First, we use paired data $\{L^i, y^i_{0}\}$ to learn the subgraph $L \rightarrow Y_0$ as a conditional Gaussian distribution (how the pendulum length affects the angular displacement). Second, we use the paired data $\{b^i, y^i_{0}, y^i_{1}\}$ to learn $(B, Y_0) \rightarrow Y_1$ as a conditional Gaussian distribution (how the damping coefficient affects the angular displacement for a fixed mass). Finally, we use the paired data $\{y^i_{1}, x^i\}$ to learn the subgraph $(Z, y^i_{1}) \rightarrow \theta$, where Z models the residual between Y_1 and the true observations θ (this subgraph is realized as a VAE). Through construction and training, the observed variable L should control the length of the pendulum, the observed variable B should control the damping coefficient, and the latent variable Z should be correlated with the mass M .² Note that while we have labeled data for the observed variables L and B , we never have access to the mass M . Despite this, the latent variable Z can still learn to model the effect of M by modeling the residual.

The results are shown in Figures 23 and 24. As can be seen, MS-VAE is able to learn completely disentangled generative factors using a combination of supervision and residual modeling. The final learned latent variable Z is shown to be heavily correlated with the mass of the pendulum, highlighting how MS-VAE’s learned latent variables can be directly related with informative physical parameters. This simple toy example highlights how MS-VAE’s training paradigm can be used to model physics-based simulators.

E FLOW-based Implementation (MS-FLOW)

As an illustration, in this section we present the MS-FLOW model on the MNIST digit dataset. Here the subgraph $C \rightarrow Y$ is realized as a Gaussian mixture model and the subgraph $(Y, Z) \rightarrow X$ is implemented as a conditional coupling flow (Dinh et al., 2016). We fit a mixture of 10 Gaussians whose means are shown in Figure 25. Figure 26 shows the real data, samples from the Gaussian mixture and the conditional flow. As expected, the log density of the overall model improves from -1585.086 to -1356.089 once the FLOW is applied to the output of the mixture model. All while maintaining the ability of controllable sampling.

²For simplicity, we don’t model the data as time series explicitly but rather as a fixed length, 1D vector.

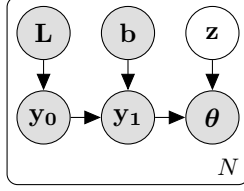


Figure 22: MS-VAE graphical model of a simple pendulum. θ is the angular displacement; L is the length; B is the damping coefficient. After learning and by construction, the latent variable Z is correlated with the pendulum’s mass.

E.1 Training using Means or Samples

As mentioned in previous sections, when training the conditional model, we can use either the means from the likelihood model of the $C \rightarrow Y$ sub-graph, or the samples from it. We fit the MS-FLOW model with both strategies and show the change of log density during training in Figure 27 Using the means makes the training converge much faster than using the samples. It is not surprised at all, because using samples leads to noisy gradients during training. Thus, for faster convergence, we use means rather than samples in all of our experiments, even though it make the estimates slightly biased.

F GAN-based Implementation (MS-GAN)

Equation 2 also allows for likelihood-free inference with a little manipulation. Simply by adding and subtracting the log of the true conditional density $\log p(X|Y)$ in equation 2, we get the lower bound,

$$\begin{aligned} \log p_{\{\phi, \theta, \theta_z, \Theta\}}(x, y) &\geq -\mathcal{KL}[q_\phi(c|y)||p(c)] + \\ &\int q_\phi(c|y) \log p_\theta(y|c) dc - \mathcal{KL}[q_{\theta_z}(z|x, y)||p(z)] + \\ &\underbrace{\int q_{\theta_z}(z|x, y) \log \frac{p_\Theta(x|z, y)}{p(x|y)} dz + \log p(x|y)}_{\text{CGAN-based } (Y, Z) \rightarrow X} \end{aligned} \quad (4)$$

Here, the log density ratio $\log \frac{p_\Theta(x|z, y)}{p(x|y)}$ can be estimated using adversarial learning with a binary discriminator function (Sugiyama et al., 2012; Srivastava et al., 2017). In practice, since we are learning conditional distributions, the decoder is implemented as a conditional GAN (CGAN) Mirza & Osindero (2014) This implementation is referred to as MS-GAN.

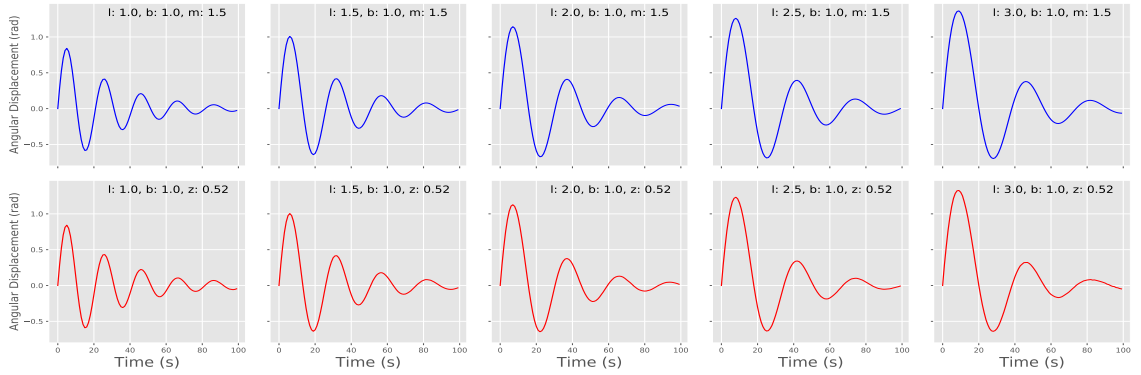
F.1 Preliminaries: Generative Adversarial Networks

Generative adversarial networks (GAN) (Goodfellow et al., 2014) represent the current state of the art in likelihood-free generative modeling. In GANs, a generator network G_θ is trained to produce samples that can fool a discriminator network D_ω that is in turn trained to distinguish samples from the true data distribution $p(x)$ and the generated samples $G_\theta(z)|z \sim p_z(z)$. Here, p_z is usually a low dimensional easy-to-sample distribution like standard Gaussian. A variety of tricks and techniques need to be employed to solve this min-max optimization problem. For our models, we employ architectural constraints proposed by DC-GAN (Radford et al., 2015) that have been widely successful in ensuring training stability and improving generated image quality.

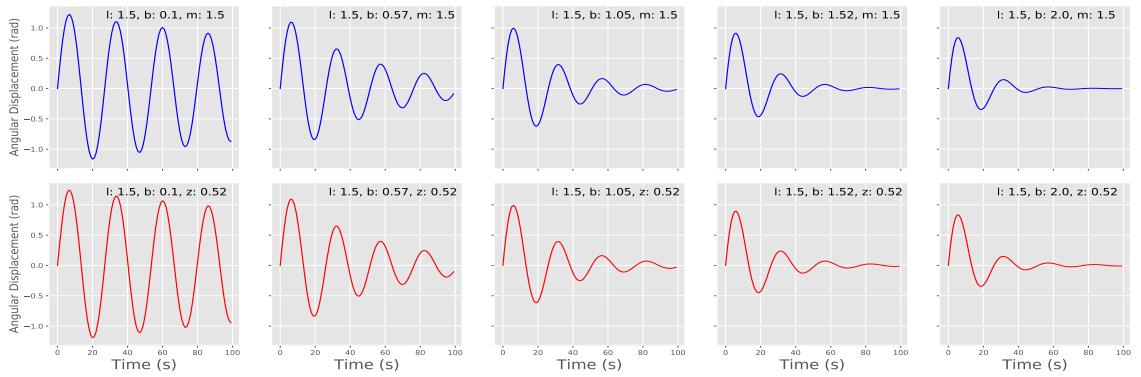
Conditional GANs (CGAN) (Mirza & Osindero, 2014) adapt the GAN framework for generating class conditional samples by jointly modeling the observations with their class labels. In CGAN, the generator network G_θ is fed class labels c to produce fake conditional samples and the discriminator D_ω is trained to discriminate between the samples from the joint distribution of true conditional and true labels $p(x|c)p(c)$ and the fake conditional and true labels $p_\theta(x|c)p(c)$.

F.2 Learning $(Y, Z) \rightarrow X$ using CGAN

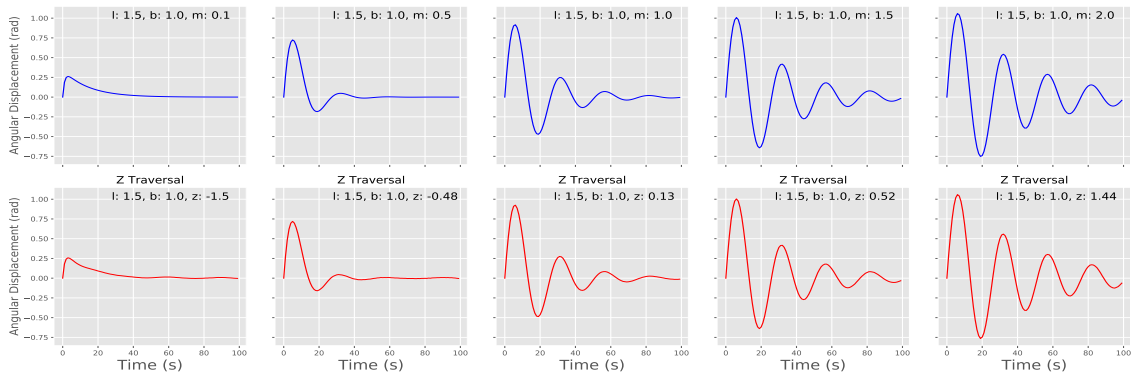
Vanilla GANs can only model the marginal data distribution i.e. they learn p_θ to match p_x and in doing so they use the input to the generator (G_θ) only as a source of stochasticity. Therefore we



(a) Traversing the length l from 1.0 to 3.0 while fixing decay constant b and z



(b) Traversing decay constant b from .1 to 2.0 while fixing the length l and z



(c) Traversing the mass m from .1 to 2.0 (top) and traversing the corresponding z values (-1.5 to 1.44) while fixing the length l and decay constant b .

Figure 23: Latent traversals for the pendulum model. Odd rows (blue) are actual data from the simulator and even rows (red) are from MS-VAE. In this example, MS-VAE learns each of the three latent variables in a disentangled manner without any supervision for the mass control variate. We choose the z values that are plotted by examining the posterior over z and choosing z values that correspond to the given masses (z is 1-Dimensional so this is straightforward).

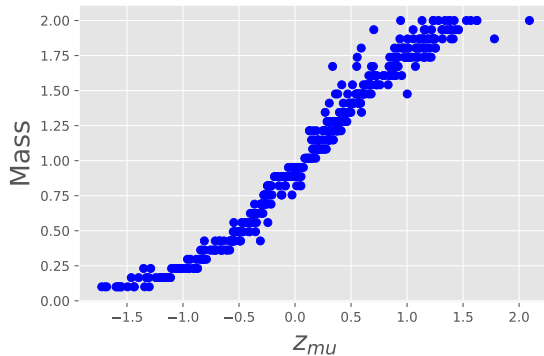


Figure 24: Correlation between z and the mass when modeling a simple pendulum. In this plot, we show 500 1-Dimensional posterior means for different θ observations to illustrate how mass and the latent variable Z are heavily correlated after training.

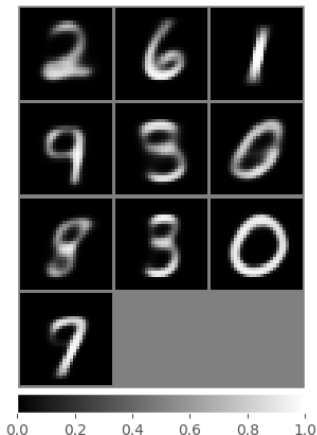


Figure 25: The means of the Gaussian mixture part of MS-FLOW on MNIST.

start with a conditional GAN model instead, to preserve the correspondence between Y and X . As shown in section F.1, this framework trains G_θ such that the observation X is maximally explained by the conditioning variable Y . One major deviation from the original model is that the conditioning variable in our case is the same type and dimensionality as the observation. That is, it is an image, albeit a blurry one. This setup has previously been used by Isola et al. (2017) in the context of image-to-image translation. With that, Z is incorporated using AdaIN as in the case of MS-VAE.

G Experiments for MS-GAN

In this section, we provide a comprehensive set of qualitative results to demonstrate how MS-GAN is clearly able to not only disentangle C from Z in both supervised and unsupervised settings but also ensure that independent components of C stay disentangled after training. Additionally, we show how in unsupervised settings MS-GAN can be used to discover disentangled latent factors when C is not explicitly provided.

We evaluate MS-GAN on a variety of image generation tasks which naturally involve observed attributes C and unobserved attributes Z . To that end, we generate three 3D image datasets of faces, chairs, and cars with explicit control variables. Chairs and cars datasets are derived from ShapeNet (Chang et al., 2015). We sample 100k images from the full yaw variation and a pitch variation of 90 degrees. We used the straight chair subcategory with 1968 different chairs and the sedan subcategory with 559 different cars. We used Blender to render the ShapeNet meshes scripted with the Stanford

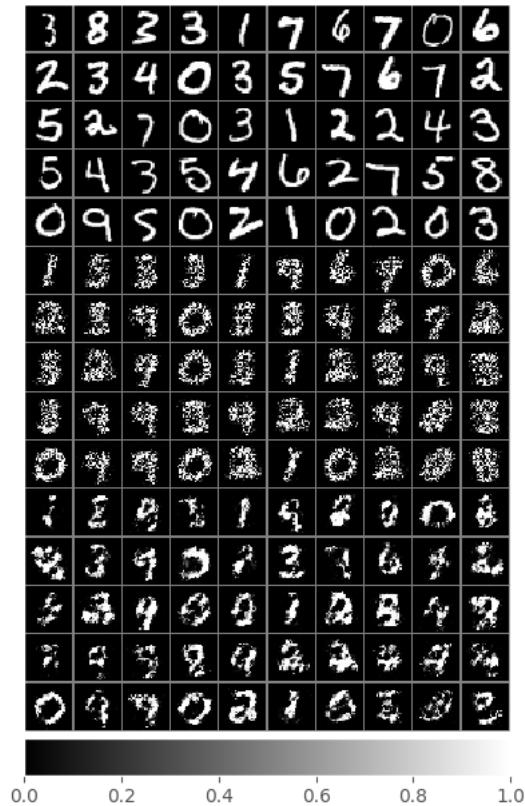


Figure 26: MS-FLOW on MNIST. First 5 rows are real data, next five rows are samples from the Gaussian mixture and last five rows are from the conditional flow.

ShapeNet renderer. For faces, we generated 100k images from the Basel Face Model 2017 (Gerig et al., 2018). We sample shape and color (first 50 coefficients), expressions (first 5 coefficients), pose (yaw -90 to 90 degrees uniformly, pitch and roll according to a Gaussian with variance of 5 degrees) and the illumination from the Basel Illumination Prior (Egger et al., 2018). For the generation of the faces dataset, we use the software provided by Kortylewski et al. (2019). For the stated datasets we have complete access to C , however, we also include unsupervised results on celebA (Liu et al., 2015) with unconstrained, real images. All our datasets are built from publicly available data and tools.

We use the DCGAN architecture (Radford et al., 2015) for all neural networks involved in all the experiments in this work and provide a reference implementation with exact architecture and hyperparameter settings at <https://github.com/AnonymousAuthors000/DS-VAE>.

G.1 Supervised Setting

In the supervised setting we compare MS-GAN to CGAN qualitatively. To evaluate the level of disentanglement between C and Z , we vary each individual dimension of C over its range while holding Z constant. We plot the generated images for both models on car and chair datasets in Figure 28. Notice that MS-GAN allows us to vary the control variates without changing the identity of the object, whereas CGAN does not. In addition, we find that for CGAN, the noise Z provides little to no control over the identity of the chairs. This is potentially due to the internal stochasticity introduced

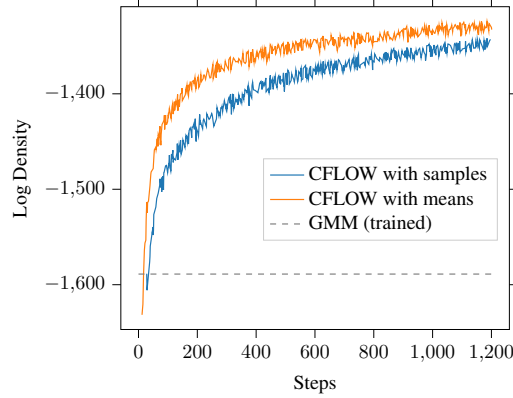


Figure 27: Conditional log density during training for different types of Y (samples v.s. means).

by the BatchNorm. The last rows for the MS-GAN figures provide the visualization of Y . It can be seen how Y is clearly preserving C (pose information) but averaging the identity related details.

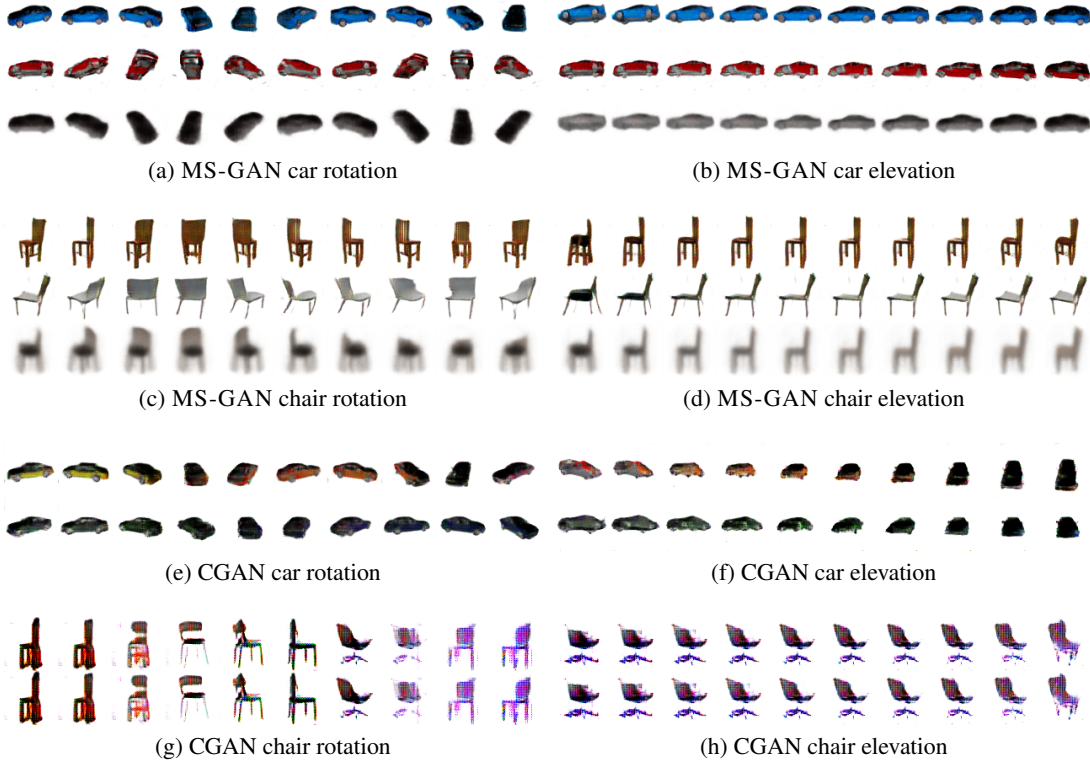


Figure 28: Latent traversal on cars and chairs. Third rows in MS-GAN results show Y .

We also qualitatively evaluate MS-GAN on the more challenging faces dataset that includes 10 control variates. As shown in Figure 32 in the appendix, MS-GAN is not only able to model the common pose factors such as rotation and azimuth but also accurately captures the principal shape component of Basel face model that approximates the width of the forehead, the width of jaw etc. Compared to CGAN, MS-GAN does a qualitatively better job at keeping the identity constant.

G.2 Unsupervised Setting

We now test the performance of MS-GAN in the unsupervised setting, where disentangled components of C needs to be discovered, using β -VAE, as part of learning the mapping $C \rightarrow Y$. For our

purpose, we use a simple version of the original β -VAE method with a very narrow bottleneck (6D for faces and 2D for cars and chairs) to extract C .

The latent traversals for the faces dataset are presented in Figure 29. Unsupervised discovery is able to recover rotation as well as translation variation present in the dataset. For comparison, we evaluate InfoGAN (Chen et al., 2016) and present the results in Figure 30 where it is evident that MS-GAN clearly outperforms InfoGAN on both disentanglement and generative quality. More traversal results are provided in the appendix. We further test our method on the CelebA dataset (Liu et al., 2015), where pose information is not available. This traversal plot is shown in Figure 31. Traversal plots for cars and chairs dataset are provided in the Figures 35 and 36.



Figure 29: Latent traversal on faces (unsupervised MS-GAN). The three latent variables capture the rotation, azimuth, and distance respectively.



Figure 30: Latent traversal of InfoGAN on faces. The latent variables are able to capture some pose changes but the pose changes are highly entangled with other pose factors as well as the face shape.

G.3 Additional experiment results

Comparison of MS-GAN and CGAN on face dataset is shown in Figure 32. CGAN not only produces blurry faces but also shows more undesired identity changes. In order to show the shape variation clearly, we provide a zoomed-in view in Figure 33.

We provide additional results for supervised and unsupervised results on the chair dataset from Aubry et al. (2014) in Figure 34 and Figure 35 respectively. The observation is the same with the previous one. MS-GAN varies the control variables without changing the shape of chairs. In the first row in Figure 34, the leg of the chairs are visually indistinguishable showing an excellent disentanglement between C and Z . For the results in unsupervised setting showing in Figure 35, MS-GAN is able to disentangle the rotation of chairs without any label.

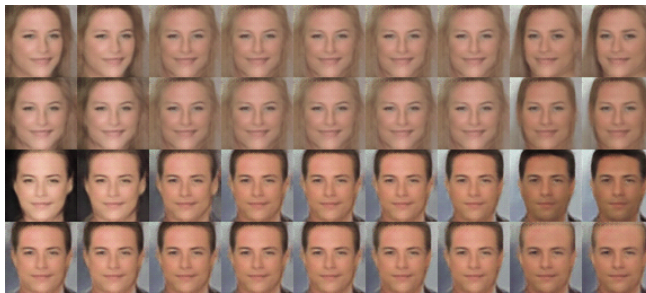


Figure 31: Latent traversal on CelebA (unsupervised MS-GAN). The latent variables consistently capture the azimuth, hair-style, gender and hair color respectively while maintaining good image quality.



(a) MS-GAN face pose



(b) CGAN face pose



(c) MS-GAN face shape



(d) CGAN face shape

Figure 32: Latent traversal of MS-GAN and CGAN on faces. The pose variations are azimuth, horizontal translation, vertical translation, distance, rotation, and elevation from top to bottom. The shape variations show the difference in face height, forehead, jaw, and ear from top to bottom.

Additional results of latent traversal of MS-GAN in the unsupervised setting is provided in Figure 36. The model is able capture the rotation but the translation is not very smooth.

Figure 37 provides the InfoGAN result on the face dataset. Compared with unsupervised MS-GAN result in Figure 38, clearly InfoGAN discovers some control variables but the effect is highly entangled.

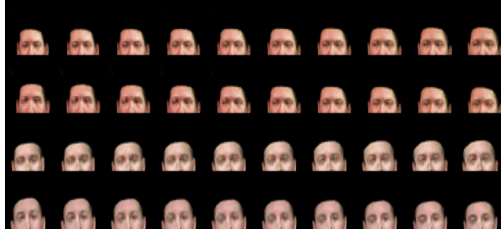


Figure 33: Zoomed-in comparison on face shape. Row 1: CGAN forehead variation; Row 2: CGAN jaw variation; Row 3: MS-GAN forehead variation; Row 4: MS-GAN jaw variation. Row 1 and Row 3 should have a bigger forehead from left to right while Row 2 and Row 4 should have a consistent forehead. CGAN and MS-GAN show good forehead variation in Row 1 and Row 3, respectively, but MS-GAN is better at keeping the forehead the same while another factor is changing (Row 4 vs. Row 1).

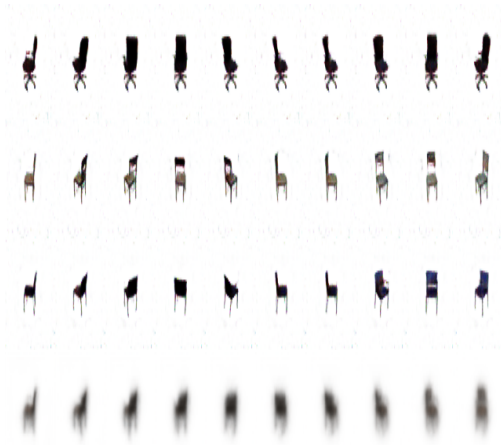


Figure 34: Latent traversal on chairs of MS-GAN. The first three rows show the effect of the variable in C that controls rotation. The last row is the corresponding Y .

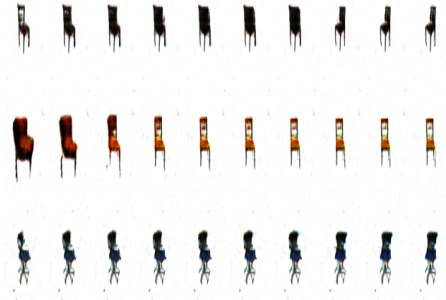


Figure 35: Latent traversal on chairs of unsupervised MS-GAN.

H Metric Formulation

The normalized mutual information (MI) reported in Figure 42a(iii) and Figure 42b(iii) is calculated as follows.

$$MI[C_R, C] = \frac{1}{n} \sum_{i=1}^n \frac{I(c^i; c_R^i)}{H(c_R^i)} \quad (5)$$

where n is the dimension of C and C_R and $I(c^i; c_R^i)$ is the mutual information between c^i and c_R^i .

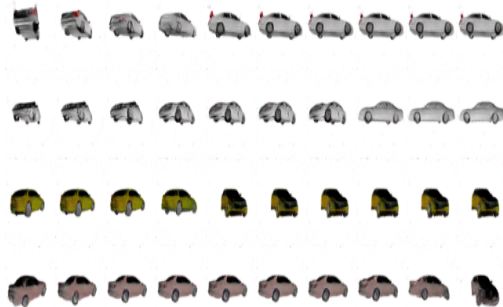


Figure 36: Latent traversal of unsupervised MS-GAN on cars.



Figure 37: Latent traversal of InfoGAN on faces dataset.

For every ground truth factor, we compute its mutual information with each one of the learned dimensions of C , normalized by its entropy. For each factor, we take the difference, in mutual information, between the top two learned variables with which it has the highest mutual information. MIG is defined to be the average of that value over all ground truth factors.

I Comparison of MS-VAE and Big- β -TCVAE

Table 4 shows the comparison of MS-VAE with Big- β -TCVAE which is a β -TCVAE that has the same capacity in terms of the number of parameters and the latent dimensionality. Our experiments reveal that MS-VAE outperforms the Big- β -TCVAE in terms of both disentanglement representation learning quality and reconstruction quality.



Figure 38: Latent traversal of unsupervised MS-GAN on face dataset.

Table 4: Comparison of MS-VAE with Big β -TCVAE.

Dataset	Model	FID	MIG
Cars	Big- β -TCVAE	35.24±1.28	0.09±0.04
	MS-VAE	22.72±3.66	0.10±0.03
SmallNORB	Big- β -TCVAE	152.19±2.68	0.16±0.02
	MS-VAE	59.16±4.52	0.22±0.01

J Sampling Multiple C and Y during Training

In our quantitative experiments for MS-VAE, the paired training set $\mathcal{D}_{\text{paired}}$ was constructed as follows: $x^i \sim p(x)$, $c \sim q_\phi(c|x)$, $y^i = \mathbb{E}_y[p_\theta(y|c)]$. In this construction, only one c and, consequentially, only one y is sampled for training. For the qualitative experiments with celebA, we sampled 10 different c 's from the β -TCVAE for each x_i such that the final dataset had 10 different y_i 's for each x_i .

The reason we sampled more y_i 's for each x_i is that there was high variability of the sampled y_i 's given the same x_i . To visualize this effect, we plot five Y samples for five X samples from a trained β -TCVAE ($\beta = 15, C = 15$) in figure 39. As can be seen from in the figure, there is high variability in the sampled y_i 's for each x_i , highlighting the the high variance of β -TCVAE's posterior distribution over C. Training with multiple y_i 's for each x_i allows the MS-VAE to naturally adapt to this variability as shown in 40. We plan to explore this effect in future work.

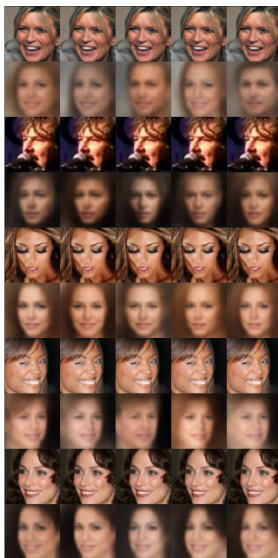


Figure 39: Even rows are samples from CelebA (the same sample is plotted five times) and odd rows are corresponding samples from the β -TCVAE. As can be seen, for the same celebA image, the reconstruction from the β -TCVAE is highly variable, illustrating the high variance of the learned posterior for β -TCVAE.

K Pixel-wise Reconstruction Loss

For all the methods, we report the L1 and L2 reconstruction errors. As shown in Figures 41 and 42, pixel-wise reconstruction loss can be misleading. In the case of SmallNorb, where MS-VAE clearly has significantly better image fidelity (as determined by the reconstruction FIDs and traversal plots), the L1 and L2 error are only slightly better than TCVAE.

L D-Separation in MS-VAE: An Illustrative Example

We provide a constructive example of the graphical model of MS-VAE shown in Figure 2c to illustrate the d-separation of Y as discussed in Section 3.1.



Figure 40: The top row is the same sample from the β -TCVAE and the bottom row is the corresponding reconstruction for MS-VAE. As can be seen in the figure, despite variability in the sampled Y 's, MS-VAE is able to reconstruct the celebA images with little variance.

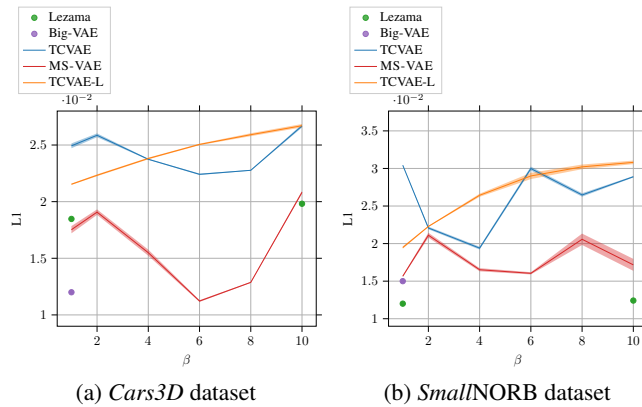


Figure 41: L1 (lower is better) comparison for β -TCVAE ($C \rightarrow Y$), β -TCVAE-L (latent dimensionality same as $C + Z$), and MS-VAE models.

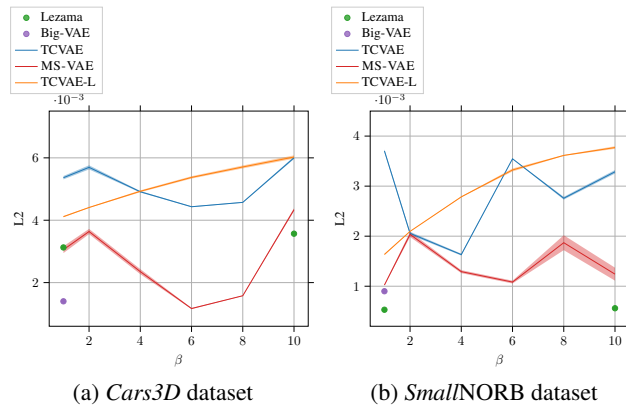


Figure 42: L2 (lower is better) comparison for β -TCVAE ($C \rightarrow Y$), β -TCVAE-L (latent dimensionality same as $C + Z$), and MS-VAE models.

Suppose we are given a dataset as shown in Figure 43d and we have trained a (disentanglement) model ($C \rightarrow Y$) where $C \sim \text{Uniform}([1, 2, 3])$ and $P(Y|C)$ is a deterministic mapping as shown in Figure 43a, where the indices above each image are the corresponding C 's. As it can be seen, only a part of dataset (first three images) are modeled by the generative process of $C \rightarrow Y$. Now, with Y generated, we add details to recover back the entire dataset. We first sample $Z \sim \text{Bernoulli}(0.5)$ and add a mask to Y . The mask is *uniformly* sampled conditionally on Z as in Figure 43b ($Z = 0$) and Figure 43c ($Z = 1$). To be more specific, e.g., given that we have sampled $Z = 0$, we apply a mask, uniformly chosen from Figure 43b to Y , which yield X . It's not hard to check that this generative

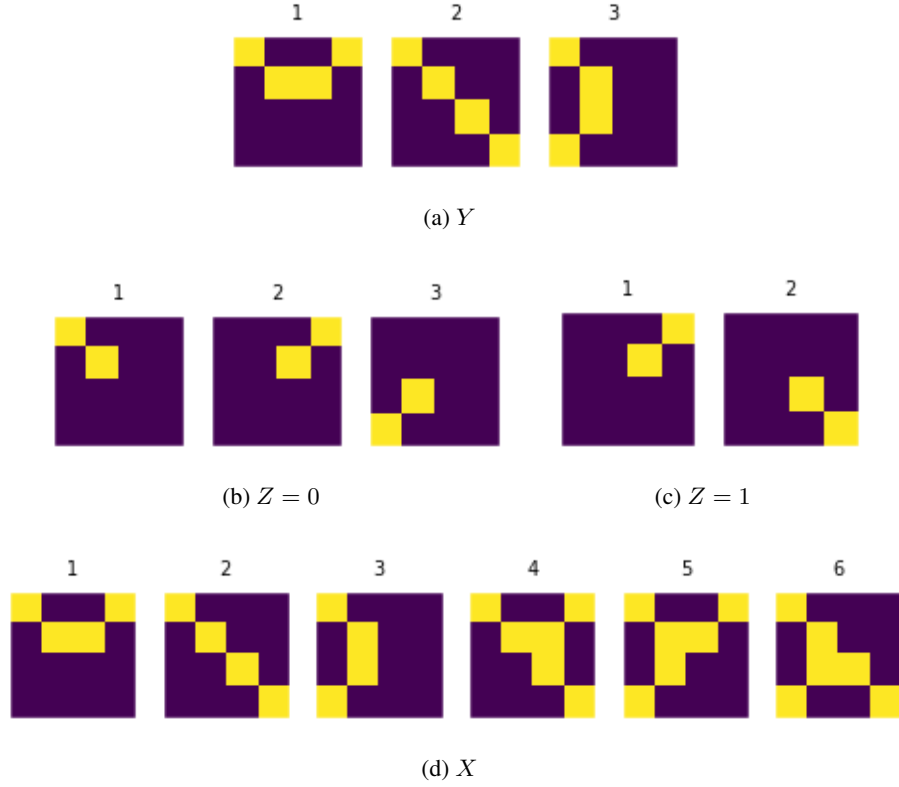


Figure 43: A constructive example to illustrate d-separation in MS-VAE.

process will yield a distribution with support shown in Figure 43d. Also, note that X and Y are in the same space. To simplify the discussion, we will represent the realizations of the random variable X and Y using the integer (C) above each image.

We want to check that C and Z are not conditionally independent given X as implied by d-separation. To do so, we pick $X = 4$ and check $P(C, Z|X = 4) \stackrel{?}{=} P(C|X = 4)P(Z|X = 4)$. The probability distributions involved here can be represented by tables, as shown in Table 5. It can be verified that

C	Z	Probability	\neq	C	Probability	\times	Z	Probability
1	0	0		1	3/8		0	1/4
1	1	3/8		2	5/8		1	3/4
2	0	1/4		3	0		(c) $P(Z X = 4)$	
2	1	3/8		(b) $P(C X = 4)$				
3	0	0						
3	1	0	(a) $P(C, Z X = 4)$					

Table 5: Conditioning on X only.

$$P(C, Z|X = 4) \neq P(C|X = 4)P(Z|X = 4).$$

Now let's check the conditional independence if we *additionally* condition on Y , e.g. $Y = 1$. Specifically, we check $P(C, Z|X = 4, Y = 1) \stackrel{?}{=} P(C|X = 4, Y = 1)P(Z|X = 4, Y = 1)$. The probability distributions involved here can be represented by tables, as shown in Table 6. It can be verified that $P(C, Z|X = 4, Y = 1) = P(C|X = 4, Y = 1)P(Z|X = 4, Y = 1)$ holds. In other words, conditioning on $X = 4$ and $Y = 1$ d-separates C and Z .

C	Z	Probability		C	Probability	×	Z	Probability
1	0	0		1	1		0	0
1	1	1		2	0		1	1
2	0	0	=	3	0			
2	1	0						
3	0	0						
3	1	0						
(a) $P(C, Z X = 4, Y = 1)$				(b) $P(C X = 4, Y = 1)$			(c) $P(Z X = 4, Y = 1)$	

Table 6: Conditioning on X and Y .

M Ablation Studies

We now report the results of the ablation studies that we conducted to understand the contribution of: 1) Our two-step training paradigm, 2) Our use of Y instead of C for the second stage, 3) Our use of AdaIN to incorporate Z , 4) Our decision to learn C before learning Z , in the following three subsections. All experiments are performed on the *Cars3D* dataset.

M.1 Importance of Two-step Training

MS-VAE uses two-step training to ensure that the disentangled factors are captured in C via the underlying β -VAE model and residual factors are captured in Z . We now show that the same will not happen if the latent space (C) of the underlying β -VAE is extended to incorporate Z and then trained in an end-to-end fashion using the same AdaIN decoder. For this purpose we train a β -VAE model (BV) with the dimensionality of C set to 5. As shown in Figure 44, BV discovers disentangled factors that capture azimuth, scale and elevation. Next, we train a model (M1) which has 10 latent factors. We enforce a higher β penalty for 5 of these latent factors (C) and a normal VAE β penalty for the other 5 factors (Z). The contribution of Z is still limited using the AdaIN decoder structure. As can be seen in Figure 44, the disentangled factors C in M1 are now entangled with other factors (e.g. identity, color). This experiment illustrates how end-to-end training cannot easily reproduce the two-step training scheme in MS-VAE which induces d-separation of C and Z .

M.2 Impact of using Y over C and AdaIN over Concatenation

MS-VAE utilizes AdaIN to improve the reconstruction Y from the underlying disentangled representation learner with information from the correlated factors Z . To understand the importance of using AdaIN (rather than concatenation) and Y (instead of C), we perform the following experiment: Using a β -VAE model (BV) as the $C \rightarrow Y$ sub-graph, we train three models MS-VAE-C (M2), MS-VAE-C-IN (M3) and MS-VAE (M4). In M2, we concatenate the inferred C with Z and use that as input to a DGM to reconstruct X . In M3, we still use the same C but introduce Z via AdaIN in the second stage DGM. In M4, we train MS-VAE as done in the paper using Y and AdaIN. In Figure 45, we show traversal plots of 4 of the disentangled factors for each of these models. For reconstruction quality, M4 outperforms both M3 and M2. This is expected as Y is produced using both C and the learned parameters of the first stage decoder θ and, therefore, contains much more semantic information about the observation X than C does. Using only C requires the second stage DGM to relearn θ while also modelling the residual between Y and X . For disentanglement, M4 and M3 both outperform M2. This illustrates how simply concatenating Z and C and inputting into the second stage DGM will result in a non-linear entanglement of the two. This entanglement causes the network to fail to condition on Y sufficiently and to use the entangled representation as a whole towards the reconstruction of X . Utilizing AdaIN to incorporate Z (as done in M3 and M4), allows the network to use Z later in the generative process to model the residual information. This allows the network to better maintain the information in Y (or C) while still incorporating Z .

M.3 Ordering of C and Z

In MS-VAE, we first learn the disentangled factors C and then we learn the residual factors Z . In this ablation, we evaluate how the order in which these latent variables are learned affects the final disentanglement. For this purpose, we train MS-VAE-ZC (M5) where, in the first stage, Z is learned

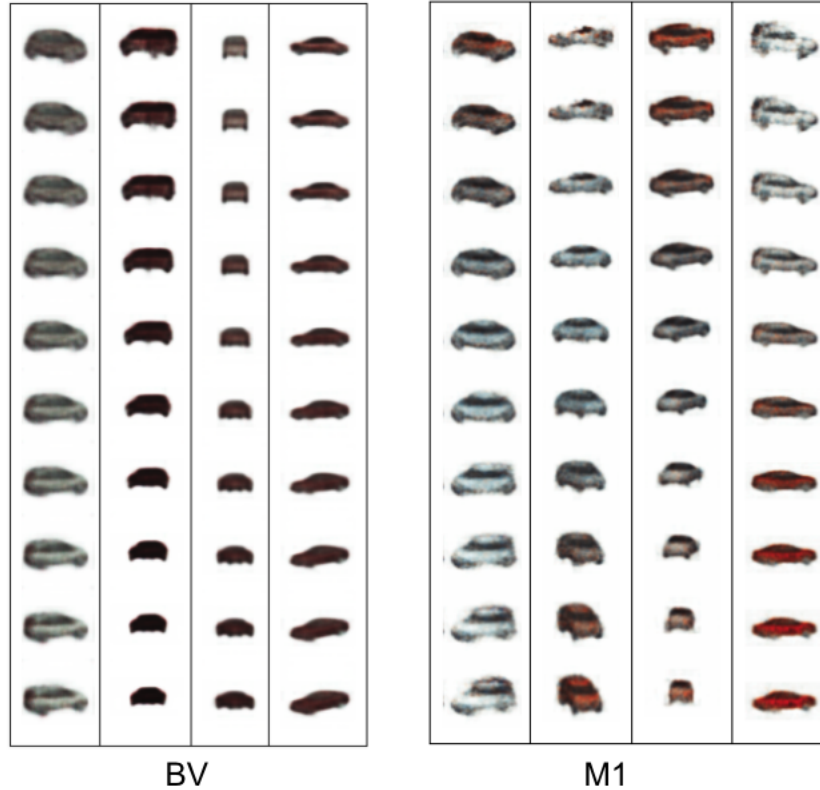


Figure 44: BV = β -VAE, M1 = β -VAE+Z. BV is trained with a dimensionality of $C = 5$. M1 is trained with a dimensionality of $C = 5$ and $Z = 5$. For M1, the β -penalty is only applied to C and Z is still incorporated using AdaIN. In this figure, we show traversals of 4 of the learned disentangled factors C for both BV and M1. As can be seen, traversing C for BV captures different disentangled factors (e.g. azimuth, scale, elevation). Traversing C for M1, however, illustrates that the disentangled factors are now entangled with other factors (e.g. identity, color).

using a standard VAE. In the second stage DGM, the disentangled factors C are learned by enforcing a KL-penalty and then concatenated with the learned Z from the first stage to reconstruct X . In Figure 46, we show traversals of 4 of the disentangled factors C . As can be seen, this new model M5 does not capture any disentangled factors in C . In contrast, MS-VAE (M4) and BV capture a variety of disentangled factors in C (e.g. Azimuth, scale, elevation). We hypothesize that M5 fails to extract any meaningful disentangled factors because Z already captured both the entangled and disentangled factors in the first part of the training. This is clearly shown in Figure 47. As such, the second stage will suffer from the shortcut problem where the decoder utilizes Z and does not learn anything meaningful in C (due to the high KL-penalty).

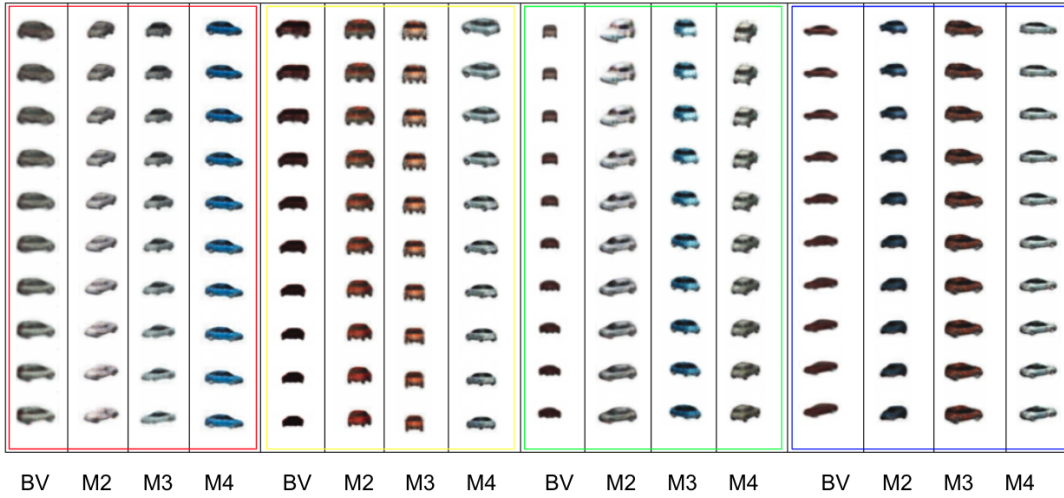


Figure 45: BV = β -VAE, M2 = MS-VAE-C, M3 = MS-VAE-C-IN, M4 = MS-VAE. BV is trained with a dimensionality of $C = 5$. In this figure, we show traversals of 4 of the learned disentangled factors and how they are preserved in each version of MS-VAE (each color box is one disentangled factor). To perform traversals for each MS-VAE, we encode X using the β -VAE to get C and Y , then we extract Z using Y ; We fix Z for the traversals of each MS-VAE. Clearly, M4 and M3 preserve the disentanglement from BV better than M2 (M2 changes the identity and color). Also, M4 has the best reconstruction of the three MS-VAE models as it utilizes Y to improve the reconstruction (rather than just using C). This ablation study illustrates that AdAIN is important for preserving disentanglement and using Y is important for improving reconstruction.

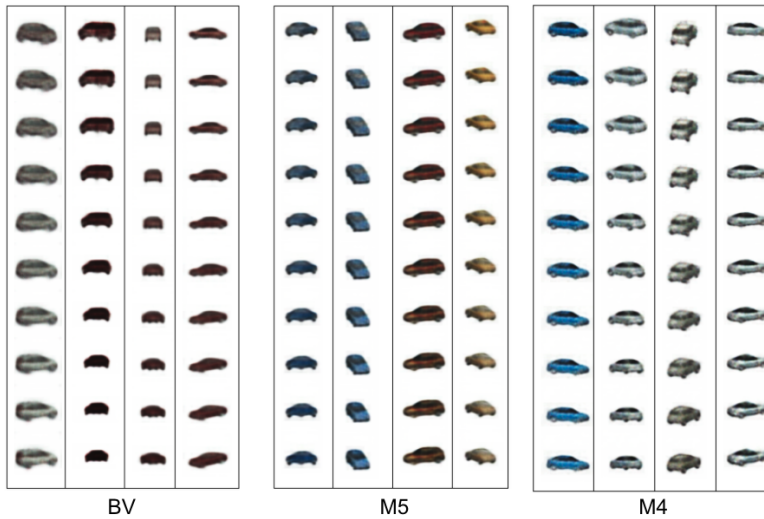


Figure 46: BV = β -VAE, M5 = MS-VAE-ZC, M4 = MS-VAE. BV is trained with a dimensionality of $C = 5$. In this figure, we show traversals of 4 of the learned disentangled factors and how they are preserved in each of the three models. To perform traversals of MS-VAE-ZC, we encode X using a VAE to first get Z and Y , then extract C using X . To perform traversals for MS-VAE, we encode X using the β -VAE to get C and Y , then we extract Z using Y . We fix Z for the traversals in MS-VAE. Clearly, M4 preserves the disentanglement from BV better than M5 (M5 as expected, is not disentangled).



M5

Figure 47: M5 = MS-VAE-ZC. In this figure, we show traversals of the Z factor in MS-VAE-ZC model. Clearly, Z is capturing factors such as scale, identity, color, rotation in an entangled fashion.

N Additional tables and plots

Table 7: Correlation between coordinates of latent vectors produced by different models and the original input features. We include all possible correlations except very low correlations, which are less than 0.2.

Coordinate type	β -TCVAE latent correlation with input	TVAE latent correlation with input		
z_1	Amount Past Due	0.218354	Balance	0.355599
			Amount Past Due	0.534584
			Delinquency Status	0.548507
			Credit Inquiry	0.485710
			Open Trade	0.426015
			Credit Inquiry_3m	0.339572
			Credit Inquiry_6m	0.457270
			Open Trade_6m	0.362006
			Delinquency Status_3m	0.566576
			Delinquency Status_6m	0.593434
	Delinquency Status_12m	0.581158		
z_2	Mortgage	0.910502	No significant correlation	
z_4	Credit Inquiry_12m	0.898419	No significant correlation	
	Open Trade_12m	0.890393		
z_5	Credit Inquiry_6m	0.808494	No significant correlation	
	Open Trade_6m	0.832294		
z_6	Utilization	0.904766	No significant correlation	
	Balance	0.879174		
	Balance_3m	0.537878		
	Balance_6m	0.428085		
	Balance_12m	0.368590		
z_7	Balance	0.358759	Balance_3m	0.285814
	Balance_3m	0.758381	Balance_6m	0.254979
	Balance_6m	0.849974	Balance_12m	0.233641
	Balance_12m	0.851672		
z_9	Credit Inquiry	0.503301		
	Credit Inquiry_3m	0.573307		
	Delinquency Status	0.725198	Credit Inquiry_6m	0.256394
	Delinquency Status_3m	0.877644	Open Trade_6m	0.209882
	Delinquency Status_6m	0.930754		
	Delinquency Status_12m	0.928545		

Figure 48: JSD comparison by features: MS-VAE versus β -TCVAE

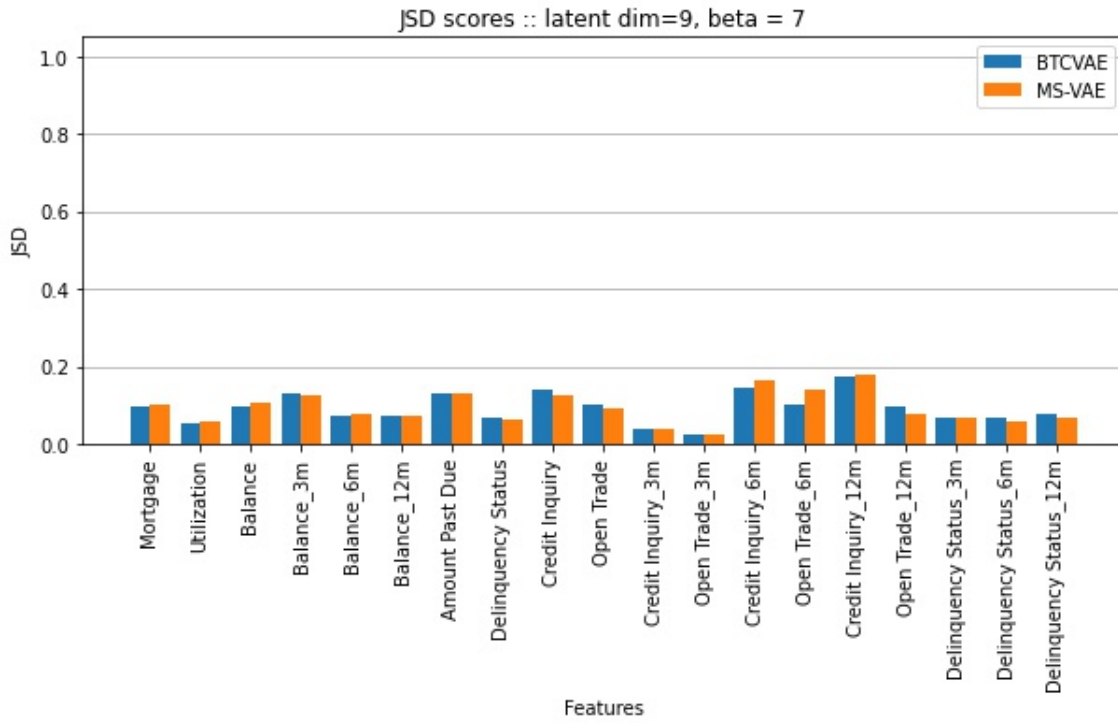


Figure 49: JSD comparison by features: MS-VAE versus TVAE

